Topics in Mechanics of Two Dimensional Crystalline Materials

by

Akbar Bagri

B.Sc., Mechanical Engineering, MUT, Iran, 2000
M.Sc., Mechanical Engineering, AUT, Iran, 2003
M.A., Chemistry, Brown University, USA, 2011

A dissertation submitted in partial fulfillment of the
requirements for the Degree of Doctor of Philosophy
in the School of Engineering at Brown University

Providence, Rhode Island
May, 2013

This dissertation by Akbar Bagri is accepted in its present form

by the School of Engineering as satisfying the

dissertation requirement for the degree of Doctor of Philosophy.

Date_____ _____

Vivek B. Shenoy, Advisor

Recommended to the Graduate Council

Date_____ _____

Pradeep R. Guduru, Reader

Date_____ _____

Brian W. Sheldon, Reader

Approved by the Graduate Council

Date_____ _____

Peter Weber, Dean of the Graduate School

Vita

Akbar Bagri was born in Andimeshk, Khouzestan, Iran on August 23, 1976. He received his B.Sc. degree from MUT, in 2000, and his M.Sc. degree from AUT, in 2003 both in Iran. He entered the solid mechanics group at Brown University for pursuing his Ph.D. degree in Fall 2008. En route to his Ph.D., he received a Masters in Chemistry from Brown University in 2011.

Acknowledgements

I would like to extend my deepest gratitude and appreciation to my advisor, Professor Vivek Shenoy. During my graduate studies, I have been privileged to work under his guidance and he has been very patient and encouraging with me throughout the course of the work.

I would also like to express my gratitude to the members of the thesis committee, Professor Sheldon and Professor Guduru for taking time out of their schedules to review and critique my work.

The fruitful collaboration with Prof. Rodney Ruoff, Prof. Manish Chhowalla, Dr. Cecilia Mattevi, Dr. Muge Acik, and Prof. Yves Chabal, is gratefully acknowledged.

I would like to thank all the current and former members of the research group of Prof. Shenoy. My thanks are due to my colleagues and friends who have helped me during the course of the work. Especially, I would like to convey my thanks to Nikhil Medhekar, Sang-Pil Kim, Rassin Grantab, Ivan Milas, Priya Johari, Hamed Haftbaradaran and Maria Stournara for their wonderful company.

I gratefully acknowledge support from the NSF and NRI through the Brown University MRSEC program and the NSF through grants CMMI-0825771 and CMMI-0855853, and the support of the Army Research Office through Contract W911NF-11-1-0171. I wish to express my sincere thanks to Patricia Capece, Peggy Mercurio, Stephanie Gesualdi, Jim Scheuerman, for their help over the years.

Finally, I would like to thank my family - my parents and my siblings who have been a source of constant support and encouragement.

Contents

List of Tables

List of Figures

Chapter 1

Introduction and overview

1.1 History of graphene

Following from the fullerenes of the 1980s and the nanotubes of the 1990s, graphene– also known as graphite layer– is one of the allotrope of carbon whose structure is a two-dimensional atomic layer of sp^2-bonded carbon atoms in a honeycomb crystal lattice [1-3]. Like diamonds and coal, graphene is made up entirely of carbon. But unlike those materials, two-dimensional arrangement of carbon atoms in graphene makes it incredibly strong and flexible. At the molecular level, it looks like chickenwire, see Figure 1.1.

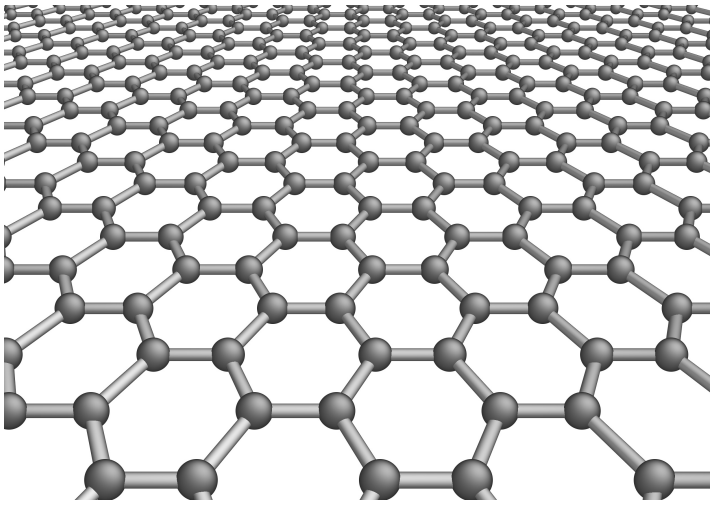

Figure 1.1: Atomic structure of graphene

Acheson [4] had developed exfoliation methods to synthesize graphite layers and these exfoliated graphite flakes have been extensively used in electronics devices as a conducting point to produce conducting surfaces in vacuum tubes [5] . In 1859, Brodie used nitric acid and potassium chromate to produce graphitic oxide, which consists graphene layers with oxygen functional groups connected to the carbon atoms [6]. Then by immersing graphite oxide into water the individual graphene oxide layers dispersed and separate layers were obtained. In 1962, using hydrazine, Boehm reduced monolayers of graphene oxide to graphene and for the first time coined term “graphene” as “ene” ending refers to hydrogen terminated edges of macromolecules of graphene [7] . Despite a long history of discovery of graphene, it took a century that graphene became important for its extraordinary electronic properties. But after work of Novoselov and Geim in 2004 [1], several research activities have been devoted to exploring the exceptional properties of graphene, including high carrier mobilities [8, 9], mechanical strength [10], optical transparency [11], and thermal conductivity [12]. Due to its extraordinary transport properties [3], it has also emerged as a promising candidate for a variety of novel applications that include nanoelectronics [13, 14], spintronic devices[15, 16], electromechanical resonators [17], impermeable atomic membranes [18], and quantum computing [19, 20]. For the realization of many of these device architectures, large sheets of defect-free graphene must be synthesized via a controlled and repeatable process. Several methods of production of grapehene have been proposed: Mechanical exfoliation, epitaxial growth on silicon carbide, epitaxial growth on metal substrates, and reduction of graphene oxide sheet. In order to guide the experimental researches, it is crucial to have a

thorough understanding of the nature of materials and their properties. In the following we briefly introduce two of these experimental methods and present the atomistic simulation methods used in present study to shed light on details of physical/chemical phenomena which are happening during the experiments.

1.2 Synthesis of graphene

1.2.1 Reduction of graphene oxide

Historically, graphene oxide (GO) reduction was probably the first method of graphene synthesis. Among the several methods that are currently being pursued, one attractive route for large-scale production and uniform deposition of graphene is solution exfoliation of graphite into individual layers [21-24]. It has been demonstrated that efficient exfoliation of graphite can be achieved via chemical or thermal oxidation to graphite oxide [25, 26]. Due to its hydrophilic nature, graphite oxide readily disperses into individual atomically thin sheets in aqueous media. Recently it has been shown that graphite oxide can be deposited in the form of thin films from solution with controllable thicknesses [23, 24, 27]. Once deposited, these films can in principle be converted to graphene by removing oxygen-containing function groups via chemical [23, 24, 27-29] or thermal reduction [30, 31]. Thus, graphite oxide suspensions provide a solution-based process for uniform deposition of graphene over large areas on a variety of substrates.

1.2.2 Epitaxial growth on metal substrates

Among the methods of production of graphene, the epitaxial growth on transition metal substrates (chemical vapor deposition method) seems to be most promising method for synthesizing large area graphene with high quality at relatively low cost. Chemical vapor

deposition (CVD) technique has been devised that exploits the low solubility of carbon in metals such as nickel [32, 33] and copper [34, 35] in order to grow graphene on metal foils. Similar to the synthesis of carbon nanotubes (CNT), the CVD growth mechanism can be understood by a vapor-liquid-solid or vapor-solid-solid model. CVD is a process whereby gaseous mixtures react, usually by an endothermic reaction to form a deposit on a heated substrate. The process generally involves the following steps: (1) initial stage (2) nucleation stage (3) growth stage until covering the whole area of metal substrate. A consequence of this technique is that the large-area graphene sheets typically contain grain boundaries, because each grain in the metallic foil serves as a nucleation site for individual grains of graphene [34].

1.3 Atomistic simulation methods

Atomic and molecular simulations can provide insights into the structural, electronic, physical and chemical properties of nanoscale structures. In recent years, with technological advancements these computational tools have been widely used to predict the properties of complex and new materials. The ability to manipulate the material at the atomic scale can lead to produce devices of unprecedented speed and efficiency. The outcome of such efforts is to revolutionize the technologies and materials in ways that will enable us to manipulate even individual atoms toward desire properties and features. The limitation of atomistic methods to simulating systems containing a small number of particles is a pathological problem in spite of continuous progress in pushing the limit toward systems of ever increasing sizes. System size is a critical issue when one desires a high degree of accuracy in modeling the inter-atomic forces between the atoms

constituting the system with quantum calculation approaches. While small size simulation is an issue for prediction of properties of bulk materials, it provides the opportunity for understanding the physical phenomena or material properties of the structures at micro/nano scales. The last decade have witnessed important theoretical and algorithmic advances in material science. Among the computational tools in materials science, Monte Carlo (MC) method, molecular dynamics (MD) and density functional theory (DFT) calculations have led to great strides in the description of materials properties. In the following, a brief review of MD method and DFT calculations, which have been used in this dissertation, is presented.

1.3.1 Molecular dynamics method

One of the promising tools in the theoretical study of materials science is the molecular dynamics method. This computational method calculates the time dependent behavior of a molecular system. MD simulations have provided detailed information on the physical/ chemical properties of structures and systems. These methods are now routinely used to investigate the structure, dynamics and thermodynamics of materials/molecules and their complexes. Alder and Wainwright first introduced the MD method in the late 1950's [36, 37] to study the interactions of hard spheres. Many important insights concerning the behavior of simple liquids emerged from their studies. Later, Rahman carried out the first simulation using a realistic potential for liquid argon [38] and the first MD simulation of a realistic system was done by Rahman and Stillinger in their simulation of liquid water [39]. The goal of this section is to provide an overview of the theoretical foundations of

classical molecular dynamics simulations which has been used in the rest of this dissertation. The general steps in MD simulations are

1) Introducing initial positions and velocities of the atoms
2) Defining the boundary conditions
3) Selection of potential energy function
4) Solving the equations of motion during an MD time span
5) Determining the thermodynamic material properties

The molecular dynamics simulation consists of the numerical, step-by-step, solution of the equations of motion, which for a simple atomic system may be written as

$$\begin{aligned} F_i &= m_i \ddot{r}_i \\ F_i &= -\frac{\partial}{\partial r_i} V \end{aligned} \tag{1.1}$$

where F_i is force exerted on atom i, m_i is mass, r_i is the position of the atom and V is the inter-atomic potential. By knowing the force on each atom and solving the equations of motions the acceleration of each atom in the system can be obtained and then using integration schemes one can determine the positions and velocities of the particles at next time step. Once the positions and velocities of each atom are known, the state of the system can be predicted at any time in the future or the past and properties of the system can be determined. Thus, in molecular dynamics simulation we need to define inter-atomic potential, which is a function of position of atoms and determines the way that particles interact with each other, and use an integration algorithm to derive the velocity and position at each time step. First, we introduce velocity-Verlet integration algorithm

used in our molecular dynamics simulations and then a brief review of different types of inter-atomic potentials will be presented.

1.3.1.1 Velocity-Verlet algorithm

In three-dimensional (3D) systems with *N* atoms, the potential energy is a function of the atomic positions with 3N variables. Due to the presence of such a complicated function in equations of motion, it would be very difficult to solve them analytically and; therefore, they are solved using numerical methods. Among the numerical algorithms developed for integrating the equations of motion, velocity-Verlet is fast and reliable and has been used in many MD simulations. The velocity-Verlet method requires current forces be calculated before the first time-step, so these routines compute forces due to all atomic interactions. Thus, the initial positions and velocities of the atoms must be defined before starting the simulations. The equations used in velocity-Verlet algorithm to compute the positions and velocities of atoms at each time step are

$$\begin{aligned} r_i(t+\Delta t) &= r_i(t) + v_i(t)\Delta t + \frac{F_i(t)}{2m_i}\Delta t^2 \\ v_i(t+\Delta t) &= v_i(t) + \frac{F_i(t) + F_i(t+\Delta t)}{2m_i}\Delta t \end{aligned} \tag{1.2}$$

1.3.1.2 Potential energy function

Selection of the potential function plays an important role in MD simulations. This selection depends on the type of materials in the system. On the other hand, potential energy used for the simulations determines the accuracy and computational time of simulations.

Pair-wise potentials

The simplest way to introduce the interaction between the particles (atoms) is to use the total potential energy of a system as a sum of energy contributions between pairs of atoms. These potential functions take the van der Waals forces into account and represent the non-bonded interactions between the atoms. Thus, they are mostly useful for rough estimation of the behavior of the systems or calculation of properties of materials where there is no bonding or weak bonds are present. Two examples of such potential are Lenard-Jones (also known as the 6–12 potential) and Morse potentials.

Many-body potentials

The development of microscopic models beyond pair potentials made it possible to describe more realistic systems. In many-body potentials, the potential energy is not defined by a simple sum over pairs of atoms interactions, but is calculated explicitly as a combination of higher-order terms. For example, embedded-atom method (EAM) [40] and tight-binding [41] potentials consider the electron density of states around each atom from sum of contributions of the atoms in the neighborhood, and then calculate the potential energy as a function of this sum. EAM potentials have been successfully used for modeling the structures, properties and defects of metals and its general form is

$$V = \sum_i \varepsilon_i(\bar{n}_i) + \frac{1}{2}\sum_{i \neq j} \phi_{ij}(r_{ij}) \tag{1.3}$$

where ϕ_{ij} is a two-body central potential between atoms i and j, r_{ij} is the distance between atoms i and j, ε_i is the embedding energy, and $\bar{n}_i$ is the electronic density of atom i due to the surrounding atoms and is defined as

$$\bar{n}_i = \sum_{i \neq j} n_i(r_{ij}) \tag{1.4}$$

in which n_i is the contribution of electronic density of atom i due to atom j at distance r_{ij}. Another example of many body potentials is Tersoff potential [42, 43], which has been used for carbon, silicon, germanium and some other materials. This potential involves a sum over groups of three atoms, and considers the angles between the atoms as an important factor. A particularly successful version of Tersoffian potential is reactive empirical bond-order (REBO) developed by Brenner [44, 45] (also known as Brenner potential), which has been widely used to model the hydrocarbons. The Tersoff potential for a system is

$$\begin{aligned}
&V = \frac{1}{2}\sum_i \sum_{j \neq i} f_C(r_{ij})\left[f_R(r_{ij}) + b_{ij} f_A(r_{ij})\right] \\
&f_C(r_{ij}) = \begin{cases} 1 & r < R - D \\ 0.5(1 - \sin[\dfrac{\pi(r-R)}{2D}]) & R - D < r < R + D \\ 0 & r > R + D \end{cases} \\
&f_R(r_{ij}) = A\exp(-\lambda_1 r_{ij}) \\
&f_A(r_{ij}) = -B\exp(-\lambda_2 r_{ij}) \\
&b_{ij} = (1 + \beta^n \zeta_{ij}^n)^{-\frac{1}{2n}} \\
&\zeta_{ij} = \sum_{k \neq i,j} f_C(r_{ik}) g(\theta_{ijk}) \exp[-\lambda_3^m (r_{ij} - r_{ik})^m] \\
&g(\theta_{ijk}) = \gamma_{ijk}\left(1 + \frac{c^2}{d^2} - \frac{c^2}{d^2 + (\cos(\theta_{ijk}) - \cos(\theta_{ijk}))^2}\right)
\end{aligned} \tag{1.5}$$

where f_R is a two-body term, f_A includes three-body interactions, r_{ij} is the distance between atoms i and j, and θ_{ijk} is the angle between bonds connecting atom i to atoms j

and *k*. The summations in the formula are over all neighbors j and *k* of atom *i* within a cutoff distance R + D. The other terms appeared in the equation are some constants that depend on type of material.

Unlike the Brenner formalism that does not include the van der Waals and Coulomb interactions that are very important in predicting the structures and properties of many systems, ReaxFF [46], which is categorized among empirical or force field (FF) potentials, uses the central force concept and takes van der Waals and Coulomb forces into account. Whereas traditional FF potentials are unable to model chemical reactions because of the requirement of breaking and forming bonds, ReaxFF avoids explicit bonds in favor of bond order, which allows for continuous bond formation/breaking. Based on a same bond order/bond distance relationship which was previously employed by Tersoff [42] and Brenner [44], ReaxFF allows for accurate description of bond breaking/bond formation and a smooth transition from nonbonded to bonded systems. The so called bond order is defined as

$$\begin{pmatrix} bond \\ order \end{pmatrix} = \frac{1}{2}\left[\begin{pmatrix} \text{number of electrons} \\ \text{in bonding orbitals} \end{pmatrix} - \begin{pmatrix} \text{number of electrons} \\ \text{in antibonding orbitals} \end{pmatrix}\right] \tag{1.6}$$

ReaxFF also contains free parameters such as atomic charges and van der Waals parameters reflecting estimates of atomic radius, and equilibrium bond length, angle, and dihedral. These parameters are obtained using some training set fittings against quantum chemical simulations. This potential has originally been developed for use in MD simulations of hydrocarbons.

1.3.2 Density functional theory calculation

Bulk structure, surface properties, kinetics and several other properties can be determined by the behavior of the ions and electrons that constitute the material. The quantum mechanics laws govern the behavior of materials and their properties. To this end, one has to solve the Schrödinger equation for the wave function ψ

$$\begin{aligned} H\psi &= E\psi \\ H &= T_n + V_{nn} + T_e + V_{ne} + V_{ee} \end{aligned} \tag{1.7}$$

where H is the Hamiltonian of the system with N nuclei and M electros, T_n is the kinetic energy of nuclei, V_{nn} is the potential energy between the nuclei, T_e is the kinetic energy of electrons, V_{ne} is the nuclei-electrons potential energy, and V_{ee} is the electron-electron potential energy. But the use of traditional quantum mechanical methods to understand the rich behavior of many particle systems is highly limited; the Schrödinger equation is analytically solvable for a few simple systems and exact solutions are available only for a small number of atoms and molecules. This is because the computational effort to solve the Schrödinger equation for a many body system grows exponentially with number of electrons. To overcome this problem, several simplifications have been made. One of these simplifications achieved by exploring the great difference in mass between the electrons and the nuclei and since the electrons move much faster than nuclei, one can assume that the nuclei are frozen in the space and solve the Schrödinger for electrons wave function only. This is known as Born-Oppenheimer approximation. But it was still difficult to solve the Schrödinger equation for a many-electrons system until Hohenberg and Kohn [47], who proved a theorem that is the basis of density functional theory

(DFT), achieved a breakthrough in the calculation of the ground state energy of the system and the derivation of a set of equations was given by Kohn and Sham [48]. The Hohenberg and Kohn theorem is: The ground-state energy from Schrödinger equation is a unique functional of the electron density. This theorem states that there exists a one-to-one mapping between the ground-state wave function and the ground-state electron density. Kohn and Sham showed that the electron density can be expressed in a way that involves solving a set of equations in which each equation only involves a single electron wave function. The Kohn–Sham equations is

$$\left(-\frac{\hbar}{2m_e}\nabla^2 + v_{eff}(r)\right)\psi_i = \varepsilon_i\psi_i \tag{1.8}$$

$$v_{eff} = v_H + v_{XC} + v_{ext}$$

where v_{eff} is the effective potential energy, v_H is known as Hartree potential which describes the Coulomb repulsion between the electron being considered in one of the Kohn–Sham equations and the total electron density defined by all electrons in the system, v_{XC} is the exchange correlation potential that defines the exchange and correlation contributions to the single electron, and v_{ext} is the potential energy due to the nuclei. The Hartree potential is

$$v_H = e^2 \int \frac{n(r')}{|r - r'|} d^3r' \tag{1.9}$$

in which e is the electron charge and $n(r)$ is the electron density defined as

$$n(r) = 2\sum_i \psi_i^*(r)\psi_i(r) \tag{1.10}$$

And v_{XC} is defined as a functional derivative of the exchange–correlation energy

$$v_{XC} = \frac{\partial E_{XC}(r)}{\partial n(r)} \tag{1.11}$$

where E_{XC} is the exchange–correlation functional appeared in energy relation. Once the single-electron wave function is obtained, the total energy that depends on the positions of ions through $v_{ext}(r)$ is obtained as

$$\begin{aligned} E[n] = -\frac{\hbar^2}{2m_e}\sum_i \int \psi_i^*(r)\nabla^2\psi_i d^3r + \int v(r)n(r)d^3r \\ + \frac{1}{2}\frac{e^2}{4\pi\varepsilon_0}\int \frac{n(r)n(r')}{|r-r'|}d^3r d^3r' + E_{ion} + E_{XC} \end{aligned} \tag{1.12}$$

Here, ε_0 is permittivity coefficient. The first term on the right hand is kinetic energy of electrons, the second term is the Coulomb interaction between the electrons and nuclei, the third term is the Coulomb interaction between the electrons, E_{ion} is the Coulomb interactions between nuclei, and the last one is the exchange-correlation term.

To find the electron density one must know the single-electron wave functions, and to know these wave functions Kohn–Sham equations must be solved. To this end, the problem is usually solved in an iterative way; the general algorithm is as follows [49]

1) Define a trial electron density, **n**(**r**).
2) Solve the Kohn-Sham equation using the defined trial electron density and find the electron wave functions, ψ_i.
3) Calculate the electron density
4) Compare the new electron density and the previous one and see if they are approximately the same. If precision condition is satisfied then the energy of the system can be obtained, otherwise one has to repeat steps 1-4 using the new

electron density until finding the correct electron density.

The practical implementation of DFT involves many techniques that have been developed through the past decades and their details can be found in DFT texts [49]. Density functional theory calculation is a phenomenally successful approach to finding solutions to the fundamental equation that describes the quantum behavior of atoms and molecules and its application is rapidly becoming a standard tool for diverse materials modeling problems in physics, chemistry, materials science, and multiple branches of engineering.

1.4 Organization of this thesis

In this thesis, we combined numerical and experimental methods to analyze the evolution of morphology of GO sheets and calculated the thermal transport in polycrystalline graphene. To this end, we have performed atomistic simulations that can shed light on properties and structural evolution of graphene and graphene oxide and guide the experimental researches. The rest of this thesis is organized as follows: In Chapter 2, we have used MD simulations to understand the atomic details of structural evolution of graphene oxide, then the MD results are validated using DFT calculations. Finally, the MD and DFT calculations are supported by FTIR and XPS measurements. In Chapter 3, we have performed MD simulations to calculate the thermal transport across grain boundaries of polycrystalline graphene and compared. We have also analyzed the effect of size and orientation of grains on thermal conductivity and boundary conductance of polycrystalline graphene. The most important results of this thesis are summarized in Chapter 4 and possible avenues for future research are discussed.

Chapter 2

Structural evolution of graphene oxide during thermal reduction process

2.1 Introduction

One of promising methods that are currently being used for large-scale production of graphene is solution exfoliation of graphite into individual layers [21-24]. It has been demonstrated that efficient exfoliation of graphite can be achieved via chemical or thermal oxidation to graphite oxide, also called graphene oxide (GO) [25, 26]. Chemically derived graphene oxide provides high yield of covalently functionalized atomically thin carbon sheets [21, 50]. GO has emerged as a solution processable material for large area electronics because it can be readily and uniformly deposited on a variety of substrates [51-53]. Various types of devices exploiting the properties of GO such as nanoelectromechanical systems (NEMS) [54], flexible transparent conductors for photovoltaics [51, 55] and thin film transistors [53] have been successfully realized. GO contains saturated sp^3 carbon atoms bound to oxygen, making it an insulator. Transition to a semiconductor via chemical or thermal removal of oxygen allows it to be incrementally reduced so that the electrical conductivity can be tuned over several orders

of magnitude [53, 56-58]. However, reduced GO (rGO) still contains residual (~ 8 at%) oxygen that is sp^3 bonded with approximately 20% of the carbon atoms [52, 56]. Presence of these sp^3 sites disrupts the flow of charge carriers through sp^2 clusters so that transport in rGO occurs primarily by hopping rather than near ballistically as in the case of mechanically exfoliated graphene [59, 60]. A clear trend between the opto-electronics properties (transparency, conductivity and mobility) has been observed with increasing sp^2 fraction via removal of oxygen in GO. However, virtually all studies in the literature using a variety of reduction techniques [52, 56, 61-63], have reported the presence of residual oxygen in rGO. Surprisingly, even extreme thermal (heating to 1373K in vacuum) and chemical reduction treatments (dipping as-synthesized GO in extremely toxic hydrazine) leads to only moderately enhanced properties with residual oxygen still remaining in sizable fractions (~ 7 at%). Therefore, the presence of residual oxygen in "reduced" GO represents a fundamental limitation that must be overcome if GO is to achieve properties resembling those of mechanically exfoliated graphene.

Crucially, knowledge regarding the bonding configuration or location of the residual oxygen is presently lacking. Thus, the atomic structure of rGO must be thoroughly elucidated so that optimum reduction process can be devised. Insight into why residual oxygen remains despite robust reduction treatments is necessary through identification of atomic positions and configurations of persistently remaining oxygen in reduced GO. Additional information regarding the density and types of defects such as vacancies that are likely to be generated during oxygen evolution as well as the final hybridization states of C-C and C-O bonds and their spatial distribution is also lacking.

A detailed spectroscopic structural analysis and opto-electronic properties of GO at different degrees of reduction has recently been reported [56] that shows the evolution of oxygen functional groups and increase in sp^2 bonding with annealing temperature. In this chapter[1], we use molecular dynamics (MD) simulations to uncover the interplay between carbon and oxygen and the degree of defects and translational order of the residual atoms at different temperatures. This atomistic level study reveals that reduction by thermal treatment leads to the formation of carbonyl and ether groups. First-principles calculations confirm that both carbonyl and ether groups are thermodynamically stable and cannot be removed by further annealing without destroying the parent graphene sheet. The MD simulation results are supported by infrared (IR) absorption and X-ray photoelectron spectroscopy (XPS) data taken in situ during the thermal annealing process. The overall results provide new insight for carefully designing reduction treatments to prevent the formation of ether and carbonyl groups to decrease the concentration of residual oxygen.

2.2 Computational and experimental methods

Graphene oxide is an atomically thin sheet of carbon [61, 66, 67], that is covalently functionalized by oxygen atoms on either side. The oxygen functional groups on the basal plane are generally thought to consist of epoxy and hydroxyl molecules [68] although evidence for the presence of ketones and phenols have been found in recent work [50]

---

[1] Significant parts of this chapter have been published in 64. Bagri, A., et al., *Structural evolution during the reduction of chemically derived graphene oxide.* Nature Chemistry, 2010. **2**(7): p. 581-587, 65. Bagri, A., et al., *Stability and Formation Mechanisms of Carbonyl- and Hydroxyl-Decorated Holes in Graphene Oxide.* Journal of Physical Chemistry C, 2010. **114**(28): p. 12053-12061.

while edges can comprise of carboxyls, anhydrates, lactones, phenols, lactols, pyrones and ketones [69, 70]. Even though a variety of models [50, 68, 71-73] have been proposed to describe this material, a coherent and detailed explanation of GO structure remains to be elucidated. GO is not stochiometric and it is highly hygroscopic [50, 74], hence its composition can vary with the synthesis method [50, 75-77] and ambient[74]. We have therefore performed MD simulations on GO sheets consisting of unit cells of 640 Carbon atoms with variable oxygen contents of 16.6% [78], 20% [78], 25% [74, 79] and 33% [75, 76, 79], values consistent with those reported in the literature.

MD simulations were performed using the reactive force field ReaxFF, which is a general bond-order-dependent potential that provides accurate descriptions of bond breaking and bond formation in hydrocarbon/O_2 systems [46].The main difference between traditional nonreactive force fields and the one that we employ in this work is that the atomic connectivity is determined by bond orders calculated from interatomic distances that are updated every MD step. This allows for bonds to break and form during the simulation. In order to account for nonbonded interactions such as van der Waals and Coulomb interactions for a system with changing connectivity, these interactions are calculated between every pair of atoms, irrespective of connectivity, and any excessive close-range non-bonded interactions are avoided by the inclusion of a shielding term [46]. The force field used in the current work was obtained by using quantum mechanics based training sets for oxidation of hydrocarbons. For simulations on a number of hydocarbon/O_2 systems [80, 81], it was found that ReaxFF obtains the energies, transition states, reaction pathways, and reactivity trends in agreement with quantum mechanical calculations and experiments.

To study the evolution of different functional groups on GO during high-temperature thermal reduction in an inert atmosphere (i.e. vacuum), we first considered a 4.3 nm × 4 nm graphene sheet with randomly distributed epoxy and hydroxyl functional groups on the two sides of the sheet. We implemented periodic boundary conditions along the graphene basal plane in order to avoid any edge effects. Once the initial groups were distributed, the GO sheet was slowly heated from 10 K to a typical the reduction temperature (in the range 1000K – 3000K) over a time span of 250 fs. The temperature of the system was obtained by applying the thermostat to the entire system, i.e. all the atoms. Therefore, according to the equipartition theorem, the kinetic energy of any given atom is 3/2 kT. Thus, local effects where reactions take place do not influence the results. It was then annealed at this temperature for a time period ranging from 25 ps to 250 ps in order to identify all possible configurations of functional groups in reduced GO. In most of our simulations, we did not find any significant change in the morphology of the sheets after the sheets were annealed for about 200 ps. Finally, in order to confirm the stability of configurations obtained as a result of high-temperature thermal reduction, rGO sheets were annealed at 300 K for 1.25 ps. These simulations were performed in a canonical NVT ensemble with a Berendsen thermostat for temperature control and a time step of 0.25 fs.

The simulated hydrogen treatment was performed on both sides of the GO sheet. The concentration of the hydrogen (H_2) was 15% of the carbon atoms in GO. The temperature was increased up to 1000 or 1500K in 250fs and held at that temperature for 50ps. The hydrogen that did not participate in any chemical reactions and any by products were then removed and the system was quenched to room temperature in 1.25ps. Finally, the system

was annealed at room temperature for an additional 1.25ps.

The first principles density functional theory calculations to compute the formation energies of epoxy, carbonyl and phenol configurations were performed with a plane wave basis set using the *ab-initio* simulation package, VASP [82, 83]. We used projector-augmented wave potentials [84] to represent the ionic cores. The generalized gradient approximation of the Perdew-Burke-Ernzerhof [85] form was employed for the exchange and correlation functional. We implemented a kinetic energy cutoff of 500 eV. To compute the total energy of the structures we used a periodic simulation cell with 120 carbon atoms with a 12 Å thick vacuum region in the direction normal to the graphene sheet. The initial structure for an epoxy group was constructed by placing an oxygen atom between two carbon atoms at a distance of 1 Å from the graphene plane, while the carbonyl pair was constructed by symmetrically placing two oxygen atoms on either side of a C-C bond at a distance of 1.5 Å from the graphene sheet. These structures were then relaxed using the conjugate gradient algorithm until the atomic forces were smaller than 0.01 eV/Å.

For the infrared absorption studies, GO samples were deposited on oxidized Si substrates (oxide ~1.5nm thick, wafer polished on both sides), with the dimensions of 3.8 ×1.5 cm (1.5 × 0.6 in). The GO thin films used for FTIR and XPS were deposited using the vacuum filtration method as reported in Ref. [53] from graphene oxide solution prepared using the modified Hummers method, details of which are also included in the supplementary information of Ref [53]. The GO-coated Si sample was held by two Ta clips (for direct resistive heating) and placed in a vacuum chamber (~10^{-5} Torr base pressure). The measurements were taken by using a ThermoFisher Nicolet 6700 FT-IR

spectrometer (KBr beam splitter) with a DTGS detector under constant nitrogen purge of 20 sccm. The optimum conditions were chosen as having an optical velocity of 0.6329 cm/sec with an incidence angle of 70° using direct transmission. The samples were heated through the current control by using 6010A DC Power Supply (0-200V/ 0-17A, 1000 W, Hewlett Packard) with a temperature control using Eurotherm. The reference for most spectra, unless specifically listed as differential spectra, is the original oxidized Si sample. Hence, any perturbation of the original oxide during GO deposition, including sample cleaning prior to deposition, is reflected in the spectra, mostly as a loss of SiO_2.

2.3 Results and discussion

The hydroxyl and epoxy groups were randomly distributed over the entire graphene sheet. However, we took into account the experimental observation of Cai et al. [86] who found that hydroxyl group bonded to a carbon atom was accompanied by an epoxy group bonded to a neighboring carbon atom, as shown in Figures 2.1a (i) and (ii). Periodic boundary conditions along the graphene basal plane were implemented to avoid any edge effects. The ratio of the hydroxyl to epoxy functional groups in the basal plane was also varied from 1:1, 3:2 and 2:3. The annealing temperatures (1000K, 1500K, 1600K and 3000K) were selected to correlate with our previous XPS study so that simulated results can be compared with experimental data. The details of the MD simulations are given in the methods section. The MD simulations were performed for 250 psec, which is two orders of magnitude longer than previously reported studies [87]. The initial configurations of GO sheets of varying oxygen concentrations hydroxyl and epoxy

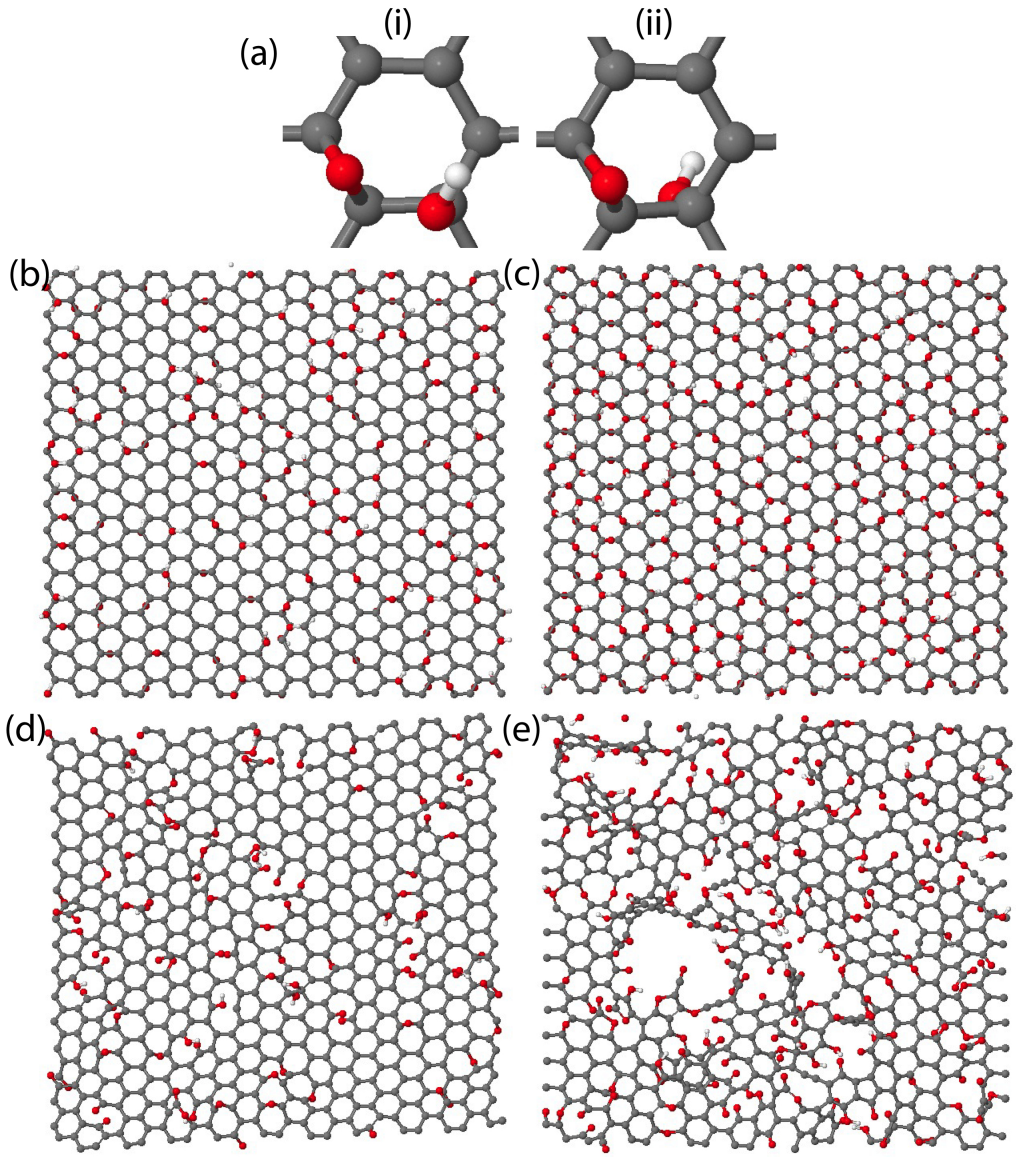

Figure 2.1: (a) Initial configuration of hydroxyl and epoxy groups used in the MD calculations based on the observations of Cai et al. [86] who found that hydroxyl and epoxy groups are bonded to neighboring carbon atoms. The hydroxyl group is shown to be on the same side of the basal plane as the basal plane in (i) while it is on the opposite side in (ii). Similarly the epoxy group can be on either side of the basal plane (not shown). Simulated GO structures for different initial oxygen contents having hydroxyl to epoxy ratio of 3:2 at 300 K. Structures for 20% and 33% oxygen contents before (b and c, respectively) and after (d-e, respectively) annealing at 1500 K are shown. Carbon, oxygen and hydrogen atoms are color-coded as gray, red and white, respectively.

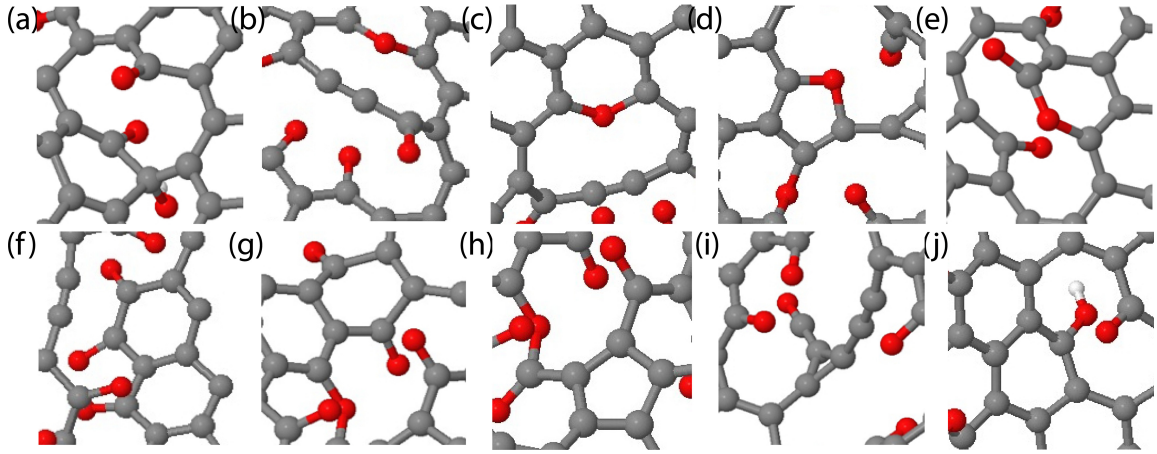

Figure 2.2: Oxygen functional groups and carbon arrangements formed after annealing: (a) a pair of carbonyls, (b) carbon chain, (c) pyran, (d) furan, (e) pyrone, (f) 1,2-quinone, (g) 1,4-quinone, (h) carbon pentagon, (i) carbon triangle, (j) phenol. Carbon, oxygen and hydrogen atoms are color-coded as gray, red and white, respectively.

groups (3:2) are shown in Figures 2.1b and c. In low oxygen content sheets, isolated functional groups can be found. As the concentration of oxygen is increased, epoxy and hydroxyl groups are in closer proximity. This leads to a dynamic interplay between the two types of functional groups during thermal annealing, which can influence the reduction process (see discussion below). In an actual GO sheet, the interactions between the functional groups play a crucial role in determining the final structure and oxygen configuration of reduced GO. The structures of the sheets after annealing at 1500K are shown in Figures 2.1d and 1e. It can be clearly observed that significant atomic rearrangement takes place and that the GO sheets are left significantly disordered after thermal annealing with the highest initial oxygen content structure being the most extreme case, as indicated in Figure 2.1e. Formation of such big holes has been reported in [88]. Specifically, carbonyls, linear carbon chains, ether rings, such as furans, pyrans, pyrones, 1,2-quinones, 1,4-quinones, carbon pentagons, carbon triangles and phenols (as

indicated in Figures 2.2a-j) along with increased sheet roughness are evident. These structural changes evolve from evolution of various functional groups with temperature. To gain insight about the morphological alterations caused by the evolution of the functional groups, we analyzed the nanoscale roughness of the carbon basal plane. The roughness of pristine GO sheet increases moderately after annealing at ~ 1500-1600K for oxygen concentrations of 20% and 25%, and dramatically for oxygen concentration of 33%, see Figure 2.3.

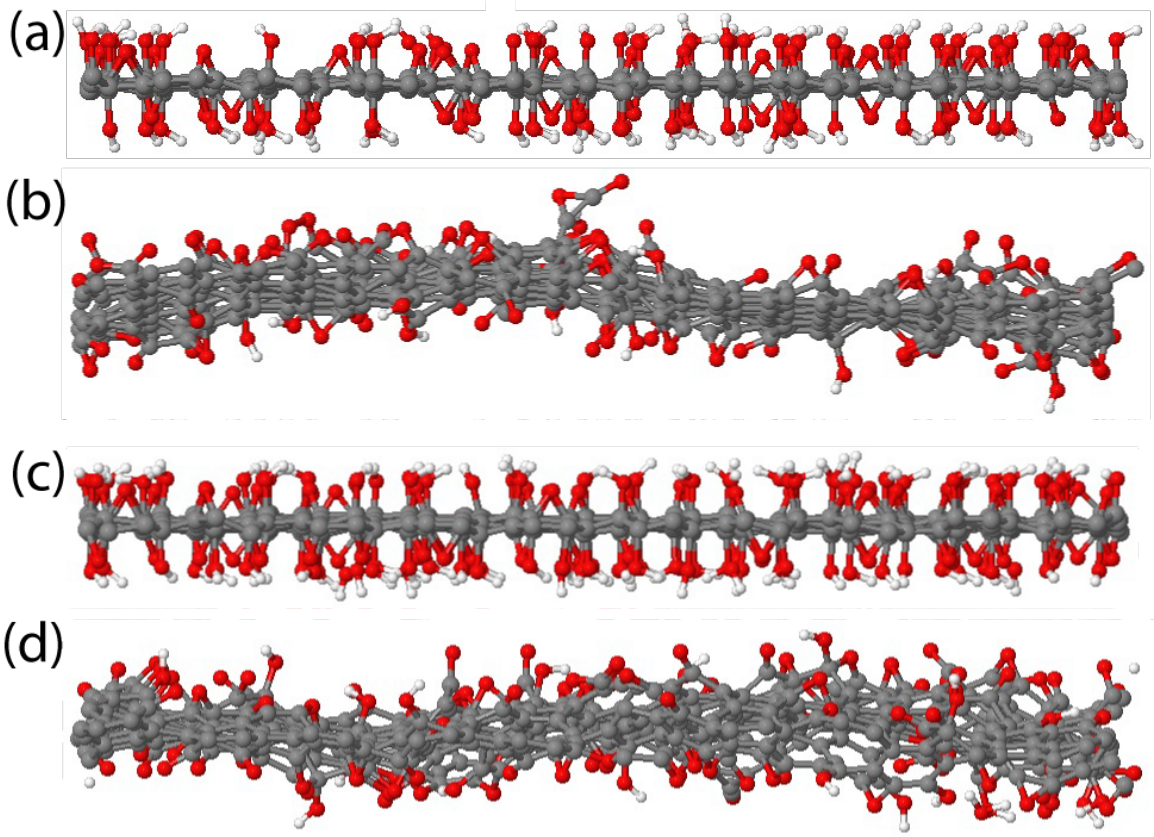

Figure 2.3: Side views of GO sheets with hydroxyl to epoxy ratio of 3:2 at oxygen concentrations of 20% (a,b) and 25% (c,d). (a) and (c) correspond to the configurations before reduction, while (b) and (d) are the configurations after reduction at 1500K.

A detailed MD simulations analysis reveals that the hydroxyl functional groups require lower temperatures for desorption than the epoxy groups, as indicated by the release of H_2O below 1000K. Above this temperature, the calculations reveal evolution of a small amount (~2%) of CO, CO_2 and O_2. The evolution of oxygen molecules are attributed to the desorption of some isolated epoxides while the release of CO_2 and CO molecules was observed when hydroxyl and epoxy sites were in close proximity, a scenario that was readily observed at the highest simulated oxygen concentration (33%) (Figure 2.1c). It is also noteworthy that desorption of hydroxyls introduces minimal disorder within the honeycomb carbon lattice, as indicated by the lower concentration of vacancies and pentagonal carbon rings these site locations (not shown). In contrast, the desorption of epoxy groups that are in close proximity to other saturated sp^3 carbon bonds, leads to the creation of vacancies within the basal plane due to the evolution of CO_2 and CO molecules above 1500K (as explained below).

Table 2.1: Simulation results of oxygen concentration after heating (1000K, 1500K) of graphene oxide with different initial oxygen concentrations. The values shown in black indicate percentage of remaining oxygen after heating (1000K, 1500K) while the values shown in red are after introducing H_2 and reheating the structure up to thermal reduction temperature (1000K, 1500K). The ratio of hydroxyls/epoxides are reported in parentheses for each initial oxygen concentration.

Initial O% / **Final O%**	**20% (2:3)**	**20% (3:2)**	**25% (2:3)**	**25%(3:2)**	**33%(2:3)**	**33%(3:2)**
1000K	18.7 (11.8)%	16.3 (8.9)%	23.1 (16.2)%	20.7 (13.3)%	29.7 (26.5)%	29.7 (23.9)%
1500K	15.4 (10.1)%	13.6 (7.2)%	20.5 (16)%	17.3 (12)%	28.9 (25.3)%	24.9 (21.6)%

The residual oxygen remaining in GO is dependent on the initial oxygen concentration, hydroxyl to epoxy ratio, and annealing temperature, as indicated in Table 2.1. The

reduction efficiency is also indicated in the Table. It can be seen that the efficiency of reduction is higher for lower initial oxygen concentrations (16.6% and 20%) and higher hydroxyl to epoxy ratio (3:2). This can be explained by the lower energy required to remove hydroxyls relative to epoxides and also from the fact that isolated epoxides are very stable (see description below). The concentration of functional groups remaining in the annealed GO versus the initial oxygen content is summarized in Figure 2.4. The percentage of remaining hydroxyl, carbonyl, ether and epoxy groups are shown as a function of initial oxygen content and annealing temperature of 1500K. It can be seen that the relative concentration of the residual hydroxyl, carbonyl, and ether groups increase at the expense of epoxy groups with initial oxygen content. It should be noted that some residual hydroxyls are present as phenols groups (Figure 2.2j), in agreement with experiments [89]. However at low initial oxygen concentration (20%), isolated epoxy groups remain even after annealing up to 1000K. In particular, at this temperature the stability of isolated epoxides can be seen by the remarkably high percentage of residual epoxide (up to 63.5% of epoxies versus only 7% of carbonyls and 0% of ethers), as shown in Figure 2.4b.

Close examination of the residual oxygen reveals that the formation mechanism of groups such as carbonyls (Figure 2.2a) and ether rings (Figure 2.2c,d), have different origins. Overall, carbonyls are created by re-arrangement of epoxide groups and hydroxyls that are closely surrounded by saturated carbons (sp^3), while substitutional oxygen (C-O-C ether rings) formation was more favored at high annealing temperatures. This is supported by the data plotted in Figure 2.4b. Considering the concentration of each functional group after relatively low temperature (1000K) annealing reported in Figure

2.4b, the carbonyls are observed to progressively increase with the initial oxygen content (from 7%-15% up to 20%-28%) whereas epoxide concentration decreases (from 40%-60% down to 37%-42%). The effect is most prominent for GO with hydroxyl to epoxy ratio of 2:3 (green filled dots in Figure 2.4b). While the increase of the initial oxygen concentration at low annealing temperatures (1000K) led to an increase in carbonyl concentration, this was much more pronounced at higher temperatures (from 1500-1600K up to 3000K), reaching a saturation value of 50%.

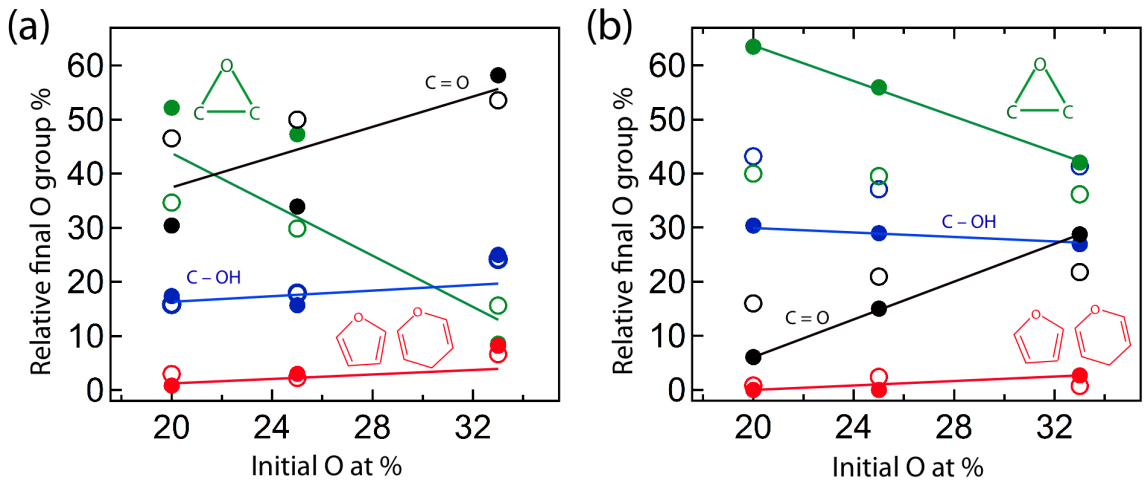

Figure 2.4: Concentrations of oxygen functional group remaining in GO after heating to (a) 1500K (b) 1000K versus the initial oxygen concentration. The different functional groups are denoted by the color: black for carbonyls, blue for hydroxyls, green for epoxides and red for furan and pyran. The filled dots indicate initial hydroxyl to epoxy ratio of 2:3 whereas the empty dots refer to ratio of 3:2. The lines are guides for the eye.

An important feature of the post-annealing morphology is that the sheet no longer remains pristine or defect-free—it is characterized by a large number of holes and other defects such as ethers along with residual epoxy and hydroxyl groups that remain on the sheet. Interestingly, the holes with carbonyl groups are distributed randomly within the GO sheet, in contrast to recent studies that suggest the presence of carbonyl groups only

on the free edges of GO sheets [90-92]. Here we focus on the formation of holes decorated by hydroxyl and carbonyl functional groups that are found in large numbers on the annealed sheets. Furthermore, we find that once these defects are formed, they are very stable against dissociation. The fact that they remain practically intact during subsequent annealing suggests that they are favorable from an energetic point of view. Next, we consider the structure and formation energies of the carbonyl- and hydroxyl-decorated holes.

By comparing the morphology of reduced GO sheets with the initial configurations of functional groups on the sheet, we have inferred that both epoxy and hydroxyl groups contribute to the formation of the hole-like defects in GO—the holes are always observed in the neighborhoods where either two epoxy groups, an epoxy and a hydroxyl group, or a cluster of hydroxyl groups were located near each other prior to annealing. Why do these holes form and what are the reaction pathways that lead to their formation starting from the epoxy and hydroxyl functional groups? To understand the preponderance of these defects in the annealed sheet, we first compute the formation energy of an isolated carbonyl pair on a graphene sheet using both the ReaxFF potential and first principles density functional theory calculations and compare it with the corresponding energy of a pair of neighboring epoxy groups.

The geometric arrangement of relaxed GO configurations consisting of an epoxy pair and a carbonyl pair are shown in Figure 2.5. By comparing the total energies of the relaxed structures, we find that both the ReaxFF and the first principles calculations predict that the configuration with a hole decorated by a carbonyl pair has lower energy than the configuration with an epoxy pair. While ReaxFF predicts that the carbonyl pair is

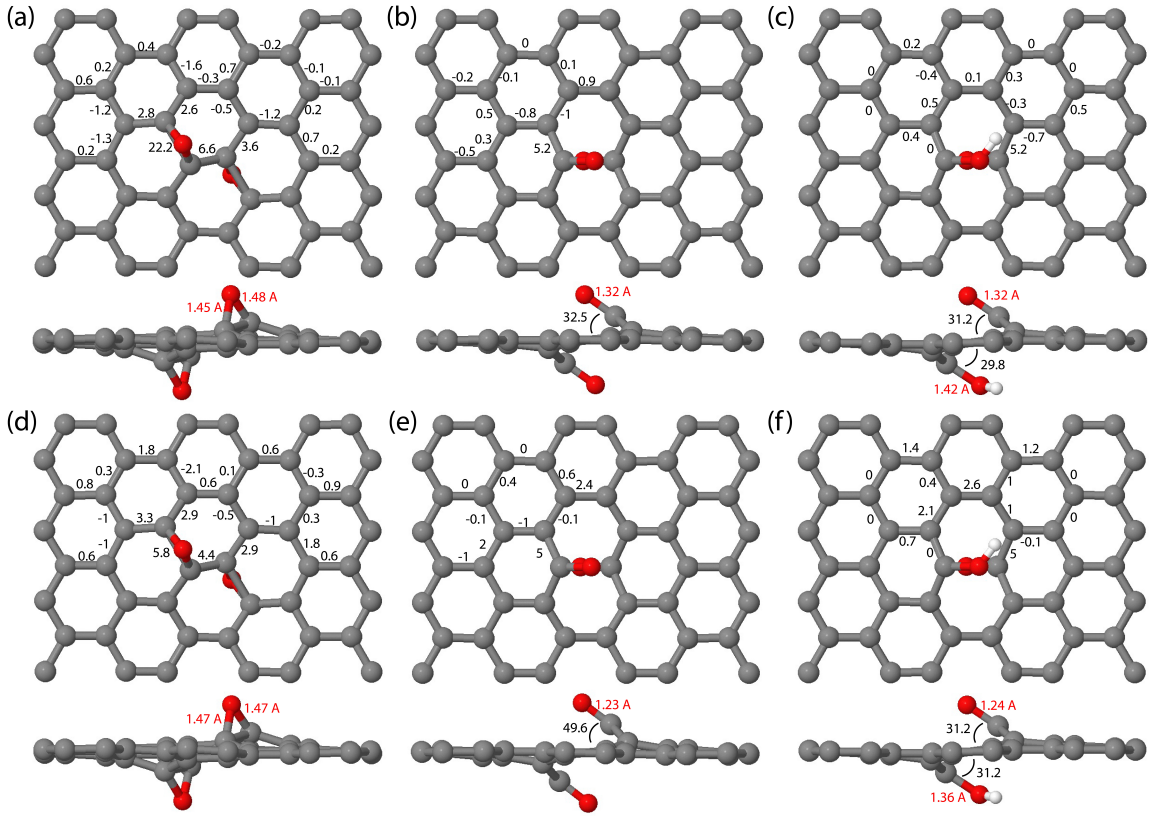

Figure 2.5: The atomic structure of relaxed GO sheets with an epoxy pair (a, d), a hole decorated by a carbonyl pair (b, e), and a hole decorated by a carbonyl and a hydroxyl group (c, f). The configurations (a-c) are obtained using the ReaxFF potential, while (d-f) are obtained by first principles methods. In each case, the strain (in %) in the C-C bonds near the functional groups is marked in the plan view (top), while the C-O bond lengths (in Å) are shown in the side view (bottom). The lengths of the remaining C-C bonds can be determined using symmetry considerations. In all the calculations, periodic boundary conditions are enforced along both coordinate directions.

favorable by 2.08 eV, VASP predicts a smaller magnitude of 0.87 eV, which is still much higher than typical thermal energies at the temperatures at which reduction is carried out. The geometric details of relaxed structures obtained by ReaxFF are nevertheless in good agreement with the first principles calculations (refer to Figure 2.5).

The relative stability of a hole decorated by a carbonyl pair can be explained by considering the strain in the basal plane induced by different functional groups. Figure 2.5 also shows the percentage change in the lengths of all graphene C-C bonds near the functional groups relative to the sp^2 C-C bonds. It can be clearly seen that the attachment of epoxy groups on graphene leads to a non-planar "frustrated" sp^3 bonding configuration for carbon atoms connected to oxygen, which in turn creates a significant strain in neighboring C-C bonds (refer to Figures 2.5a and 2.5d). However, in the case of a hole with a carbonyl pair, the bonding configuration remains close to planar sp^2 hybridization due to the formation of carbon-oxygen double bonds (C=O), leading to small strain in the basal plane as shown in Figure 2.5b) and Figure 2.5e. A hole with a carbonyl pair is therefore a relatively strain-free structure resulting in a lower formation energy compared to the epoxy pair.

In the above analysis, we restricted attention to a particular placement of the epoxy groups. Next, we show that a hole with a carbonyl pair is *lower* in energy than *any* pair of epoxy groups. Figure 2.6 shows the relaxed structure and the energy of several arrangements of these groups obtained by ReaxFF, including the case where the epoxies are placed on two sides of a C-C bond (refer to Figure 2.6a). From the computed energies of these configurations, it is clear that the formation of the carbonyl pairs is favorable over all other arrangements—the energy of the carbonyl pair is lower than all other configurations by 2 eV or more.

It is also interesting to note that the formation energy of the pair of epoxies attached to the same carbon atoms (one epoxy group on each side of the sheet) in Figure 2.6a is the least favorable compared to all other arrangements including two non-interacting epoxies

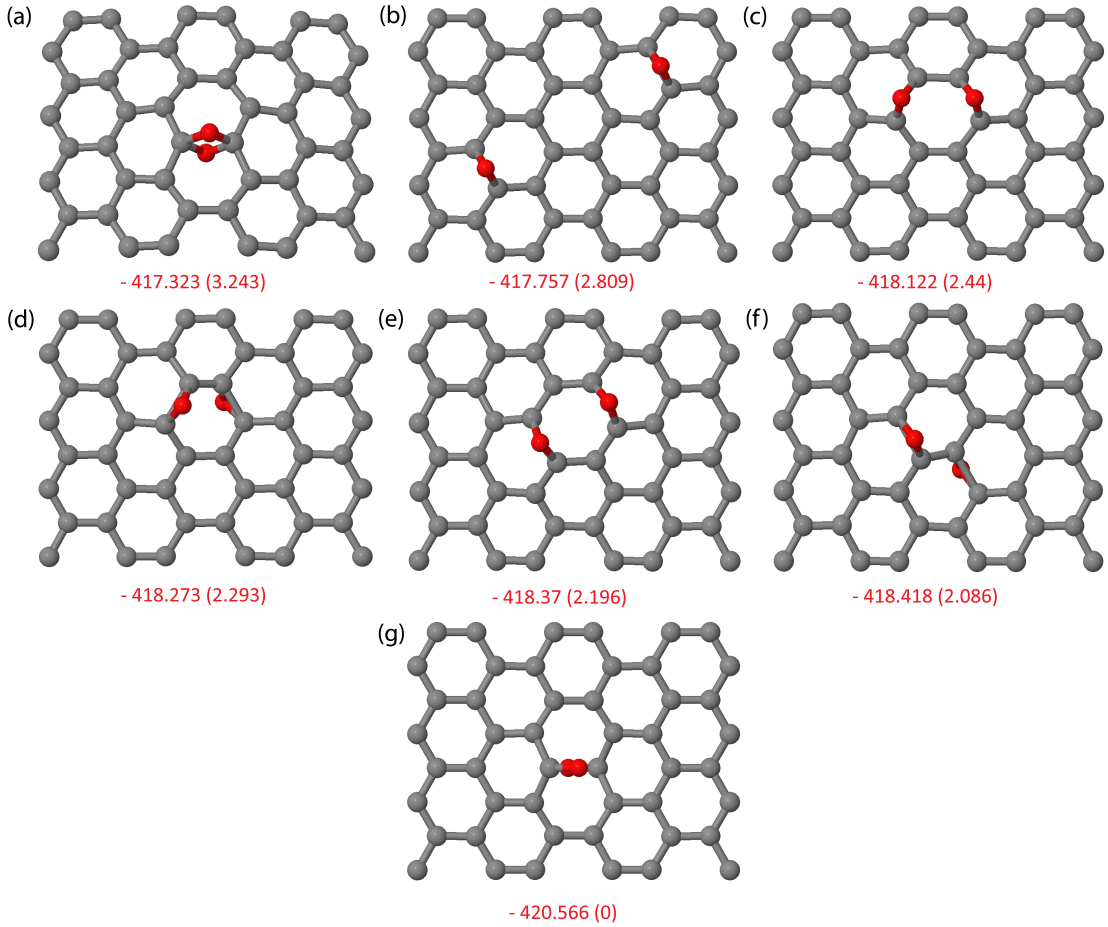

Figure 2.6: The potential energy map – as predicted using ReaxFF – for the relaxed GO sheet with pairs of epoxy and carbonyl groups arranged in different configurations. For each configuration, the absolute potential energy of the system in eV is given, while the energy relative to state (g), the lowest energy configuration, is noted in parentheses.

located far from each other. On first glance this result is somewhat surprising, particularly in light of very recent work [93] that shows that it is indeed favorable to attach a new epoxy group to existing epoxy groups. To understand the cause for this discrepancy, it is important to recognize that the formation energies of the epoxy groups depend strongly on the arrangement of other functional groups in their vicinity. Based on the computed formation energies, we find that the attachment of a new epoxy group that

is already a part of an “epoxy row” is indeed favorable over the attachment of an epoxy far from this row (the energy is lowered by 0.4 eV as shown in Figure 2.7). On the other hand, the attachment of a new epoxy group to an existing but isolated epoxy group increases the energy by 0.43 eV compared to attaching the new epoxy far from the existing epoxy, as shown in Figures 2.6a and 2.6b. An epoxy group leads to the stretching of the underlying C-C bond to 1.78 Å and 2.42 Å when it is in isolation and part of an epoxy chain, respectively. When a new epoxy group is added in the former case, this bond has to be further stretched, which can only by accomplished by creating a significant strain in the other bonds in the vicinity.

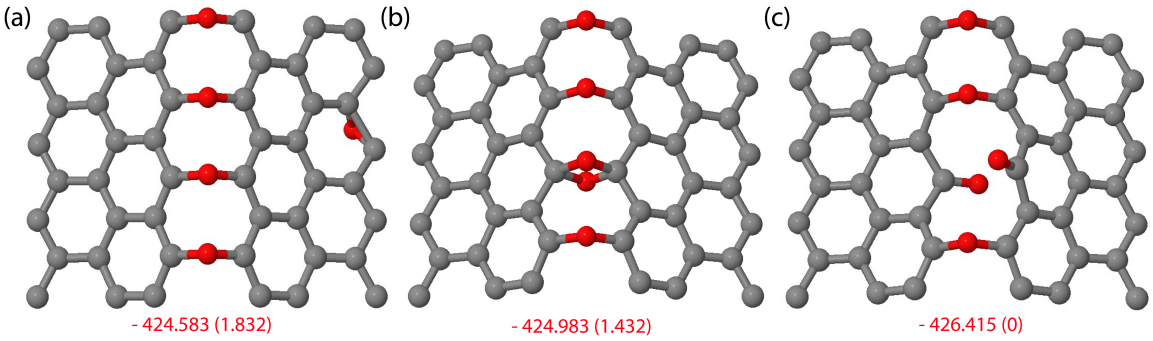

Figure 2.7: The potential energy map for graphene oxide with a row of ethers and an epoxy group (a,b), and a row of ether and a carbonyl pair (c), as predicted using the ReaxFF potential. For each case, the absolute potential energy of the system in eV is given, while the energy relative to state (c), the lowest energy configuration, is noted in parentheses. The relative energies of these configurations are in qualitative agreement with an earlier first principles study [93].

It should also be pointed out that the hole formation mechanism proposed in Li. et al [93]. relies on the existence of a row of epoxies, see Figure 2.7. However as pointed out by Ajayan and Yakobson [94], it is not clear how isolated epoxy groups fall into ranks to

take part in a well orchestrated serial bond-breaking and rebonding process that leads to the formation of the epoxy rows. The randomly-bound epoxy groups can only find such stable alignments as a result of rapid vacillation between different sites, but this is not easy to reconcile with the high energy barriers associated with such a mechanism, which can be of the order of 1 eV [95]. In distinct contrast to holes formed at the epoxy chains, the holes formed in our simulations arise solely from the random arrangement of epoxy and hydroxyl groups.

In Figures 2.5c and 2.5f we consider the relaxed structure of a different hole-like configuration—a hole decorated by a carbonyl and a hydroxyl group; based on these calculations, it is evident that the formation of a hole decorated by a carbonyl and a hydroxyl group also leads to small strain in the basal plane. While the ReaxFF calculation predicts that the structure with a hole decorated by a carbonyl and a hydroxyl is lower in energy by 1.09 eV compared to the configuration with a hole, first principles calculations reveals no major difference between the energy of these configurations. For this structure, first principles calculations show that structure without a hole is lower by 0.06 eV than the structure with a hole. Next we describe in detail the reaction pathways and the mechanisms that lead to the formation of holes during thermal reduction of GO.

Now, we elucidate bond-breaking and formation mechanisms by which carbonyl- and hydroxyl- decorated holes are created on GO. Based on our molecular dynamics simulations of large GO sheets, we have identified three different mechanisms for the formation of holes in GO sheets during thermal reduction. To systematically study these mechanisms, we have arranged the initial configurations that lead to hole formation on small GO sheets (1.3 nm × 1 nm, or 48 carbon atoms in the basal plane). For each

mechanism of hole formation, we analyze the variations in the bond lengths and bond orders of the bonds near functional groups. By monitoring these quantities, we can identify the key steps in the sequence of events that lead to the formation of holes and estimate the energies of ephemeral transition states. In what follows, we show that the specific initial distributions of epoxy and hydroxyl groups essentially facilitate the breaking of C-C bonds and subsequent tearing of the sheets by creating large strain in the basal plane.

In each case, the initial configurations were first created by placing hydroxyl or epoxy functional groups adjacent to each other as shown in Figures 2.8a, 2.10a and 2.12a. These configurations were subsequently relaxed using the conjugate gradient algorithm until the atomic forces were less that 0.01 eV/ Å. The relaxed structures were then slowly heated from 0 K to a typical reduction temperature of 2000 K over a period of 250 fs, following which they were annealed until the transformation of the initial structure into a configuration with a hole was observed. As in the case of thermal reduction of a large GO sheets shown in Figure 2.1, we employed a canonical NVT ensemble with a Berendsen thermostat [96] for temperature control and a time step of 0.25 fs. In order to understand the influence of annealing temperature, this procedure was repeated with different annealing temperatures in the range 700 K to 2000 K. In all the cases, the key events in the formation of holes (such as transfer of atoms between adjacent functional groups and bond dissociation) were observed essentially at all the temperatures—the frequency of such events was merely found to be greater at higher temperatures. Finally, by computing the potential energies of the initial and final relaxed structures in each case, we confirm

that the final configuration is indeed energetically favorable compared to the initial configuration.

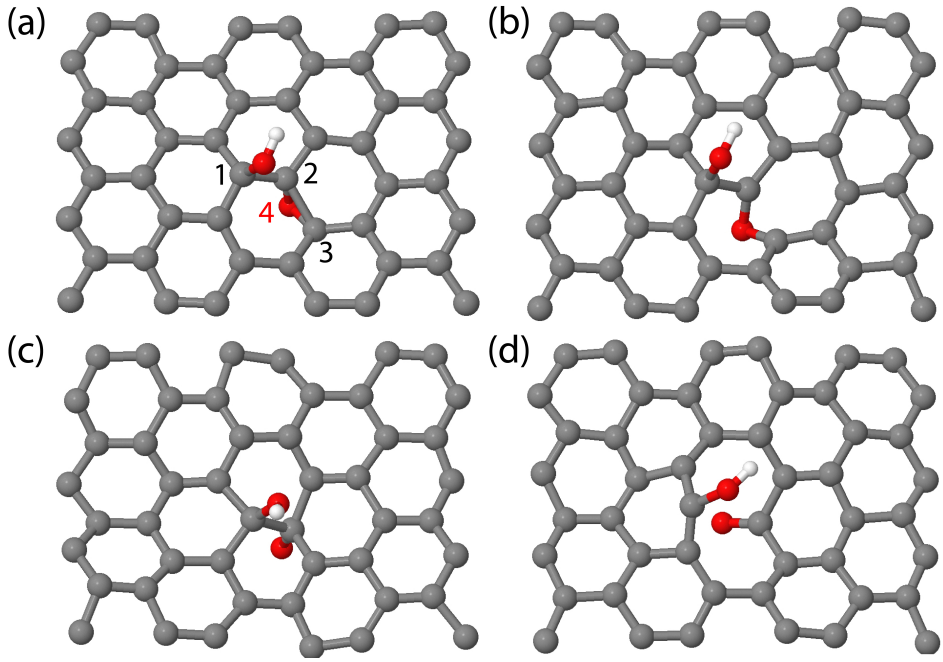

Figure 2.8: Hole formation in GO due to the interaction of epoxy and hydroxyl groups during thermal reduction at 2000 K. The snapshots present a chronological evolution of the structure at 3.5 ps, 3.6 ps, 4.0 ps, and 4.25 ps. Carbon, oxygen and hydrogen atoms are color-coded as gray, red and white, respectively.

1. Hole formation due to interaction of epoxy and hydroxyl groups

The first mechanism that we consider involves an epoxy group and a hydroxyl group located on opposite sides of the basal plane, as shown in Figure 2.8. In equilibrium (Figure 2.8a), these groups create significant distortion of the C-C bonds in their vicinity as evidenced by the bond orders and bond-lengths in the configuration shown in Figure 2.9a—the bond lengths between the atoms C1-C2 and C2-C3 in Figure 2.8a are close to 1.55 Å (compared to 1.44Å for C-C bonds in graphene) while their bond order of approximately 1 indicates a bonding configuration that is closer to an sp^3 bond rather than

the sp^2 bonding in graphene. Upon annealing, the events that lead to the formation of the hole in the graphene sheet (in Figure 2.8d) can be identified as follows:

1) Stretching of the C2-C3 bond: As the simulations progress, we find that the C2-C3 bond undergoes large oscillations in bond length, stretching up to 1.77 Å (22% stretch) indicating that the lattice distortion induced by the arrangement of functional groups leads to significant weakening of this bond. We find that the stretching of this bond acts as a precursor to the creation of holes.

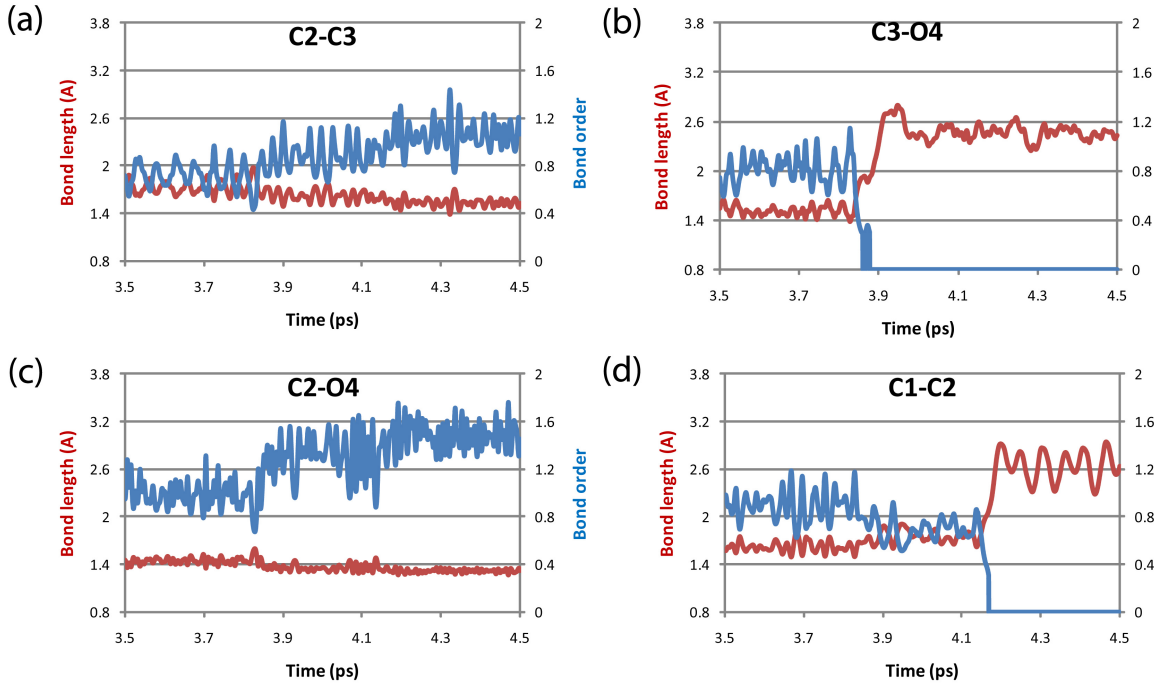

Figure 2.9: Variations in the bond lengths and bond orders of the most relevant bonds during hole formation in GO due to the interaction of epoxy and hydroxyl groups given in Figure 2.8. C1, C2, C3, and O4 correspond to the carbon and oxygen atoms marked in Figure 2.8a.

2) Breaking of the C3-O4 bond: The stretching of the C2-C3 bond also influences one leg of the epoxy bonds, namely C3-O4. As the carbon atom C2 is also part of the nearly

tetrahedral bonding arrangement (arising from the presence of the hydroxyl group on the atom C1), the C2-O4 bond does not stretch to any significant degree. On the other hand, we find the C3-O4 bond undergoes oscillations of larger amplitude and breaks, leading to a double bond between C2-O4 (as evidenced by the bond order of 1.5 in Figure 2.9c) yielding an intermediate high energy configuration. The potential energy of this intermediate configuration is approximately 0.75 eV greater than the configuration shown in Figure 2.8a.

3) Breaking of the C1-C2 bond: The breaking of the bond C3-O4 also facilitates further out-of-plane distortion of the carbon atoms C1 and C2 resulting in an increase in bond length from 1.55 Å to 1.75 Å and the reduction in bond order from 1 to 0.7 as seen Figure 2.9d. The weakened C1-C2 eventually breaks, creating a hole in the sheet (Figure 2.8d) that is decorated by a carbonyl and a hydroxyl group on the two sides of the sheet. This configuration remains stable upon further annealing. We find that the potential energy of this configuration is favorable over our initial configuration by 1.1 eV.

2. Formation of holes by interaction of hydroxyls

Here we consider holes that can be formed by the interaction of pairs of hydroxyls connected to the two sides of the sheet as shown in Figure 2.10. Here, we find that the bond between carbon atoms C1 and C2 is stretched to 1.7 Å —a 17% increase in bond length compared to the sp^2-connected carbon atoms (see Figure 2.11a). Upon annealing this configuration, we observe the following sequence of events that lead to the formation of a hole with a carbonyl pair along with the release of two water molecules.

1) Breaking of the C1-C2 bond: As the sheet is annealed, the C1-C2 bond oscillates between 1.5 Å and 1.8 Å until it eventually breaks, as shown in Figure 2.10b.

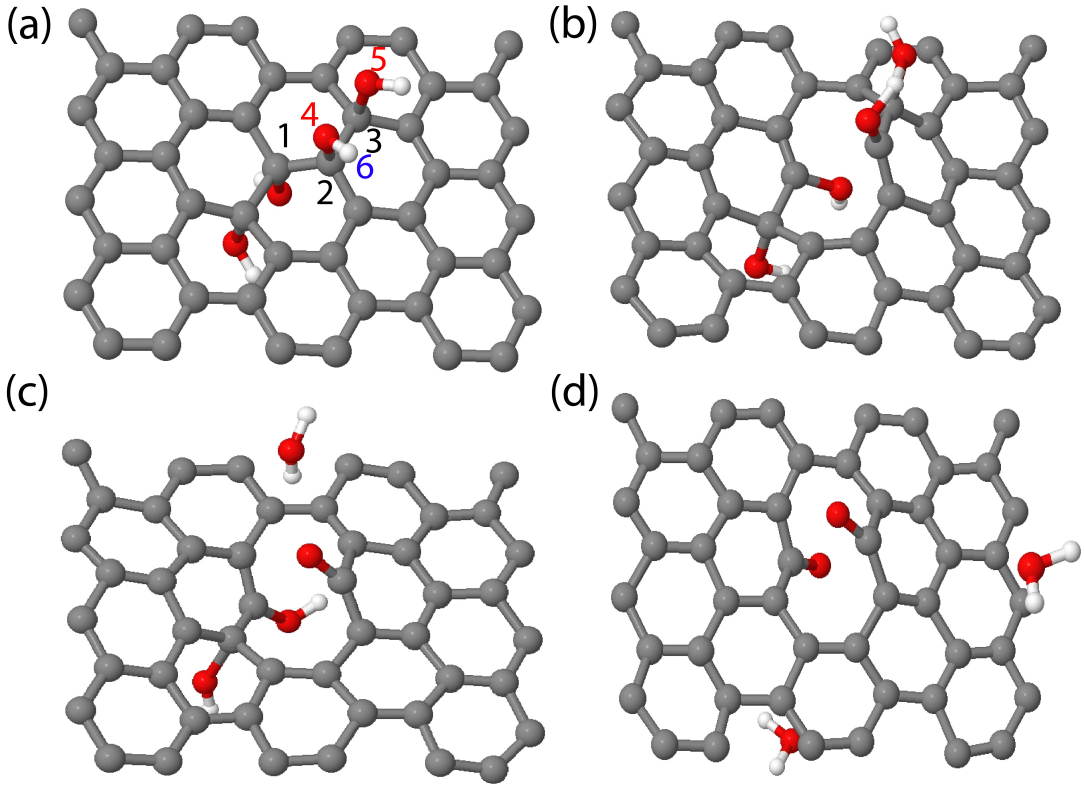

Figure 2.10: Hole formation in GO due to the interaction of hydroxyl groups during thermal reduction at 2000K. The snapshots present a chronological evolution of the structure at 0.75 ps, 1.0 ps, 1.1 ps, and 3.5 ps. Carbon, oxygen and hydrogen atoms are color-coded as gray, red and white, respectively.

2) Formation of water molecule via hydrogen bonding: Once the C1-C2 bond breaks, to satisfy the electron valence, the bond order between these carbon atoms and the connected oxygen atoms increases. For example, as seen in Figure 2.11b, when the C1-C2 bond breaks, the bond order between C2 and O4 increases from 0.9 to 1.3. This essentially weakens the bond between the oxygen and hydrogen atoms in the hydroxyl groups (for example, O4-H6). The eventual dissociation of the hydroxyl group (O4-H6)

is facilitated by weak hydrogen bond interactions between the adjacent hydroxyl groups (see Figure 2.10b). As a result of these interactions, the hydrogen atom H6 migrates to the neighboring hydroxyl group, leading to the formation of a carbonyl group and a water molecule. The newly formed water molecule eventually escapes the sheet as indicated in Figure 2.10c. In a similar manner, the hydroxyl group connected to the carbon atom C1 also dissociates via the mechanism discussed above, giving rise to the carbonyl pair and an additional water molecule as shown in Figure 2.10d.

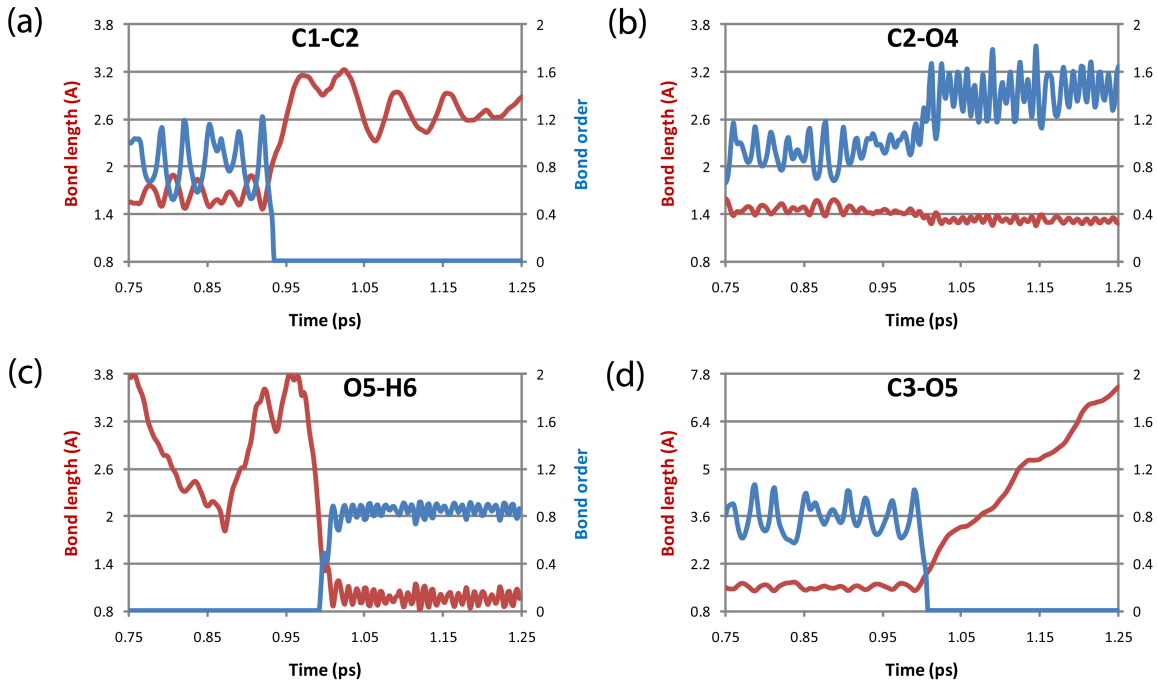

Figure 2.11: Variations in the bond lengths and bond orders of the most relevant bonds during hole formation in GO due to the interaction of hydroxyl groups given in Figure 2.10. C1, C2, C3, and O4, O5 and H6 refer to the carbon, oxygen and hydrogen atoms marked in Figure 2.10a.

The final structure with the carbonyl pair is energetically favorable—the combined potential energy of this structure and the water molecules is lower by approximately 0.2 eV compared to the configuration in Figure 2.10a. We note that, if there is only one

hydroxyl group on one side of the sheet shown in Figure 2.10a, it will give rise to one water molecule and a hole decorated by a carbonyl and a hydroxyl group—a configuration very similar to the one which forms as a result of the interaction between an epoxy group and a hydroxyl group shown in Figure 2.8. Finally, we find that the energy difference between the initial configuration and the state where the C1-C2 bond is stretched to 1.8 Å (Figure 2.10b) to be 1 eV, which provides an estimate for the energy barrier for hole formation.

3. Hole formation due to interaction of epoxy groups

Figure 2.12 demonstrates the formation of two holes and two carbonyl pairs from the neighboring epoxy groups. As discussed earlier, epoxy groups on graphene sheets alter the bonding environment in their vicinity and give rise to significant deformation of the sheet. The degree of distortion depends on the relative positions of the groups. For example, for the configuration in Figure 2.12a, where two neighboring epoxy groups are connected to the opposite sides of the graphene sheet, the carbon bonds C1-C3 and C1-C2 are stretched by 17.5% compared to the sp^2 bonds in graphene. Below we discuss how carbonyl pairs are created as this structure is annealed.

1) Breaking of the C3-O5 bond and the formation of a lone oxygen bond: The sequence of reactions that transform neighboring epoxy groups to a carbonyl pair begins with the weakening of bonds C1-C3 and C3-O5 (refer to Figure 2.12b). As a consequence of large local strain and thermal fluctuations, the bond C3-O5 breaks, resulting in a high-energy intermediate configuration with carbon atom C1 connected to three neighboring carbon

atoms as well as the lone oxygen atom O5 (refer to Figure 2.12c). We estimate that the potential energy of this configuration is greater than the configuration shown in Figure 2.12a by approximately 0.75 eV.

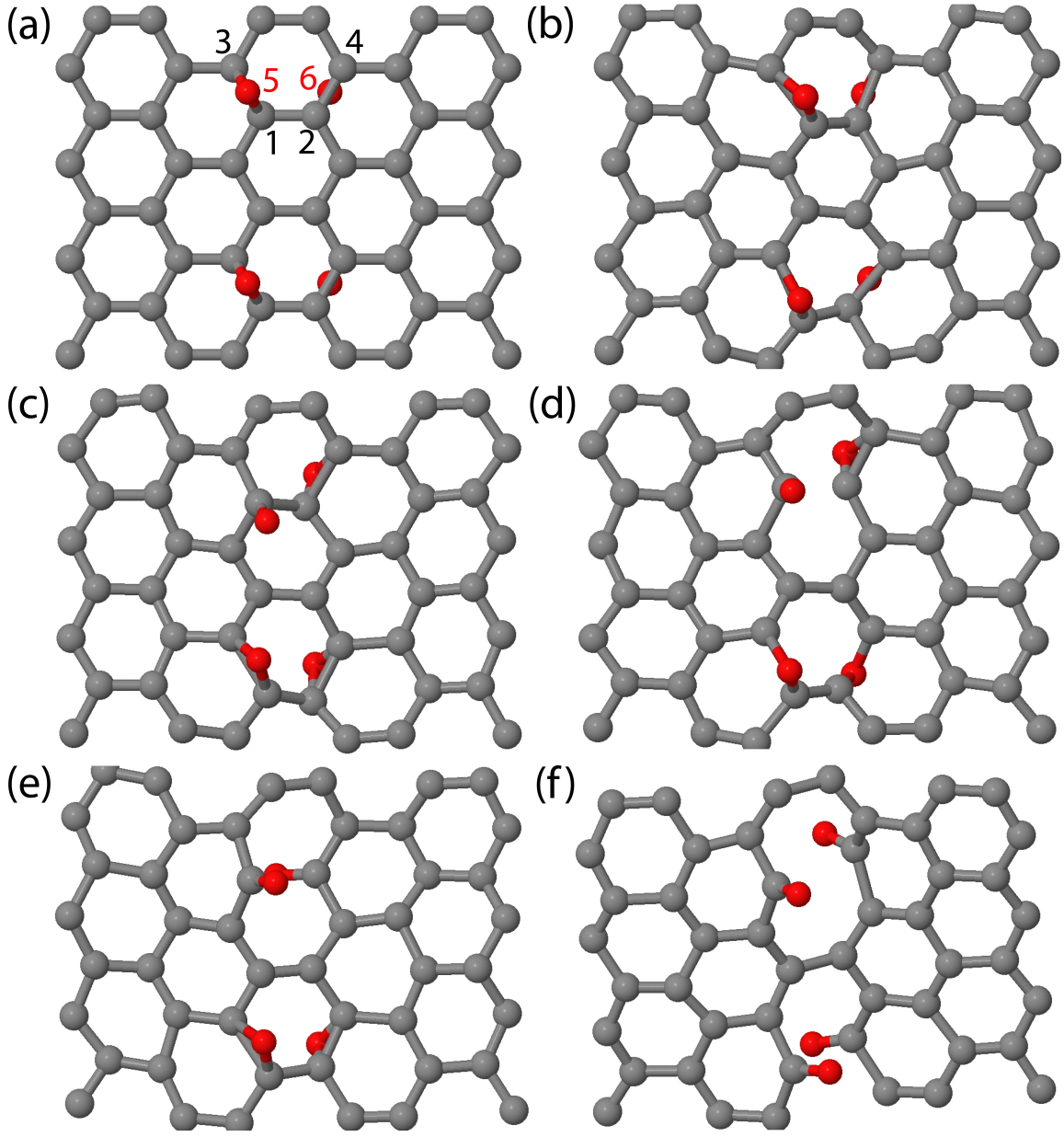

Figure 2.12: Hole formation in GO due to the interaction of epoxy groups during thermal reduction at 2000 K. The snapshots present a chronological evolution of the structure at 0.4 ps, 0.55 ps, 0.7 ps, 1.12 ps, 1.2 ps and 5.0 ps. Carbon and oxygen atoms are color-coded as gray and red, respectively.

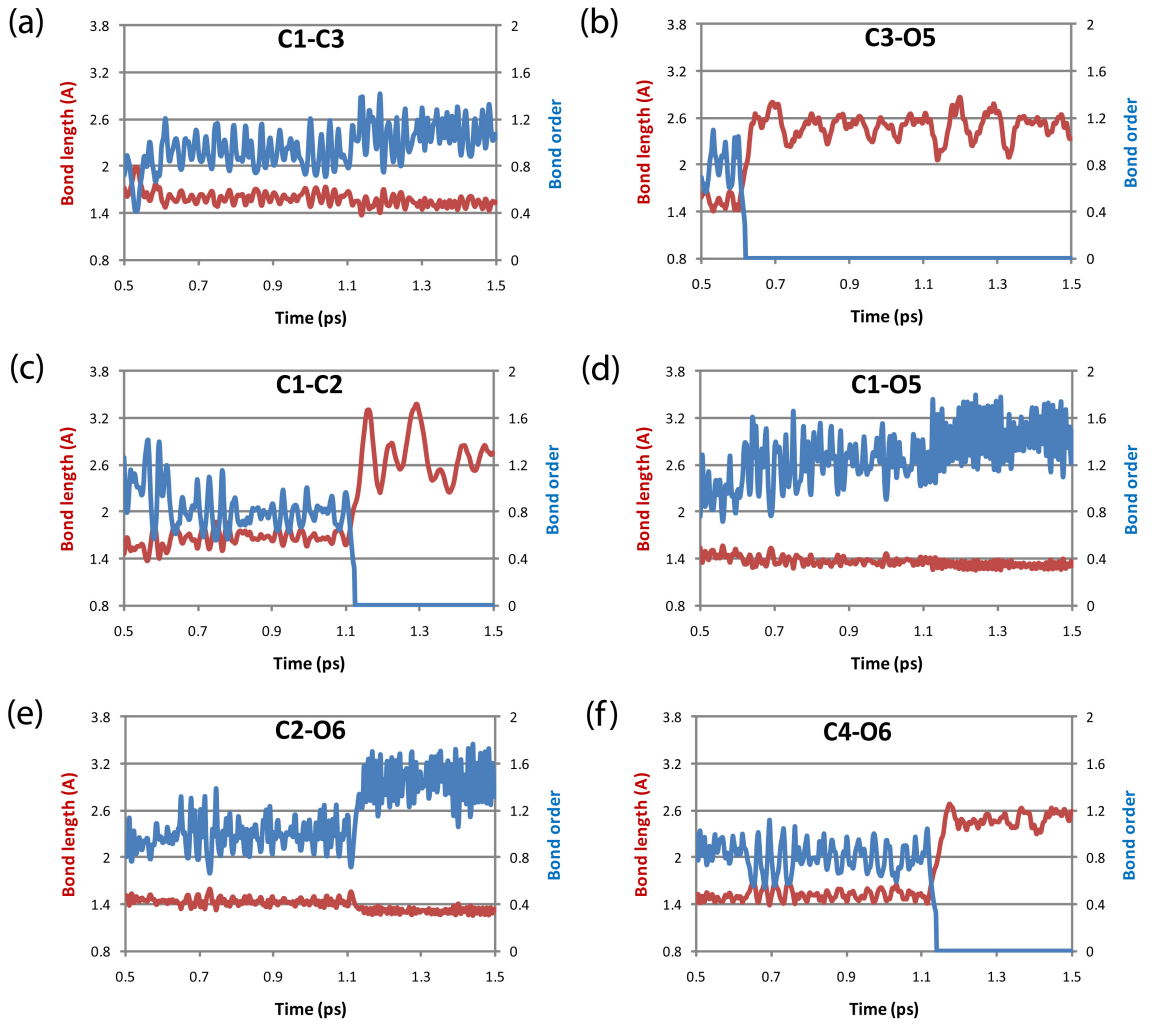

Figure 2.13: Variations in the bond lengths and bond orders of the most relevant bonds during hole formation in GO due to the interaction of epoxy groups given in Figure 2.12. C1, C2, C3, C4 and O5 and O6 refer to the carbon and oxygen atoms marked in Figure 2.12a.

2) Breaking of the C1-C2 bond and the formation of a carbonyl group: The high-energy configuration with the lone oxygen bond gives way to a lower energy configuration (Figure 2.12d) by breaking the strained C1-C2 bond, as evidenced from the sudden decrease in the bond order shown in Figure 2.13c. As soon as the bond C1-C2 breaks, the

bond order for C1 and O5 increases to 1.5 (see Figure 2.13d), denoting the formation of a carbonyl group. In the end, the neighboring epoxy group C2-O6-C4 also transforms to a carbonyl group resulting in a configuration with a hole decorated by a carbonyl pair, as shown in Figure 2.12e. The formation of this configuration is indeed energetically favorable—the energy is lowered by 2.3 eV as a result of the transformation from a pair of neighboring epoxies to the carbonyl pair. The second pair of epoxies shown in Figure 2.12a also transforms to the carbonyl pair shown in Figure 2.12f via the mechanism discussed above.

We note that the mechanisms for the creation of holes in graphene oxide that we have discussed here do not involve any migration of functional groups along the graphite sheet—the holes are created solely as a consequence of local bond dissociation and reformation. This feature is in contrast to an earlier molecular dynamics study [97] where the formation of holes was observed to be preceded by the migration of epoxies along the graphene sheet at high temperatures. Finally, our molecular dynamics simulations reveal that a different arrangement of epoxy groups in the initial configuration in Figure 2.6f, where the neighboring epoxy groups are located on the neighboring hexagonal ring instead of the same hexagonal ring in Figure 2.8a, also yields a pair of carbonyl groups via the same mechanism discussed above.

As discussed above, the formation of carbonyls can be linked to the interplay between hydroxyl and epoxy groups or to two epoxides bonded with two neighboring carbon atoms and facing opposite side of the sheet. The four different initial configurations of the oxygen groups that lead to formation of carbonyl- and hydroxyl- decorated hole-like configurations are summarized and shown in Figure 2.14. The generation of carbonyls in

such configurations is thermodynamically favored as evidenced by the reduction in the total energy (as indicated by the corresponding energy values given for each transition computed using first principles calculations described in the methods section) of the system upon formation of these functional groups (Figure 2.14).

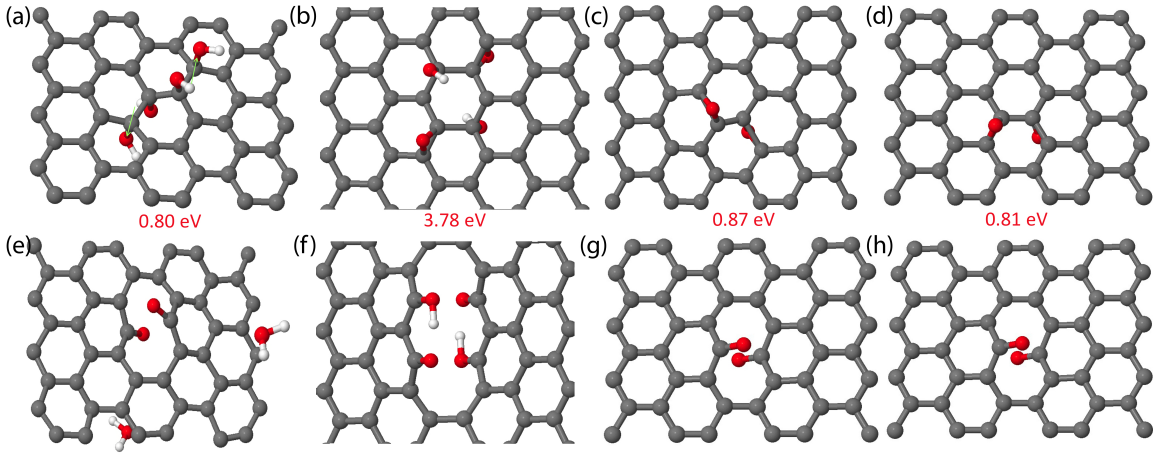

Figure 2.14: Initial configuration of hydroxyl and epoxy groups (top) leading to formation of carbonyl and hydroxyl decorated holes (bottom). In (a) transfer of hydrogen between neighboring hydroxyl groups (indicated by arrows) leads to the formation of a carbonyl pair. In (b-d) strain created by epoxy groups leads to the creation of carbonyl and phenol groups that relax the strain the neighboring carbon atoms. The energy difference ($E_i - E_f$ in eV) between the initial configurations (top) and the final configurations (bottom) in each case obtained using DFT calculations (refer to methods section for details). Note that formation of these holes is energetically favorable in all cases. Carbon, oxygen and hydrogen atoms are color-coded as gray, red and white, respectively.

The attachment of epoxy groups on graphene leads to a non-planar "frustrated" sp^3 bonding configuration for carbon atoms connected to oxygen, which in turn creates a significant strain in neighboring C-C bonds, enhancing their IR activity (IR absorption by the C-C stretch modes at ~1550 cm^{-1}). However, in the case of a hole with a carbonyl pair, the bonding configuration remains close to planar sp^2 hybridization due to the

formation of carbon-oxygen double bonds (C=O), leading to small strain in the basal plane. The transition states along with energy barrier of creation of these carbonyl-phenol- decorated holes are shown in Figure 2.15. These calculations are performed using the nudge-elastic band (NEB) method implemented in VASP [82, 83]. The nudged elastic band (NEB) is a method for finding saddle points and minimum energy paths between known reactants and products. The method works by optimizing a number of intermediate images along the reaction path. Each image finds the lowest energy possible while maintaining equal spacing to neighboring images. This constrained optimization is done by adding spring forces along the band between images and by projecting out the component of the force due to the potential perpendicular to the band.

Multiple interactions between several hydroxyl and epoxy groups, especially for high initial oxygen contents (25%, and 33%), can also lead to stable highly oxygenated hexagons, such as pyrones, 1,2-quinones and 1,4-quinones (Figures 2.2e-g).

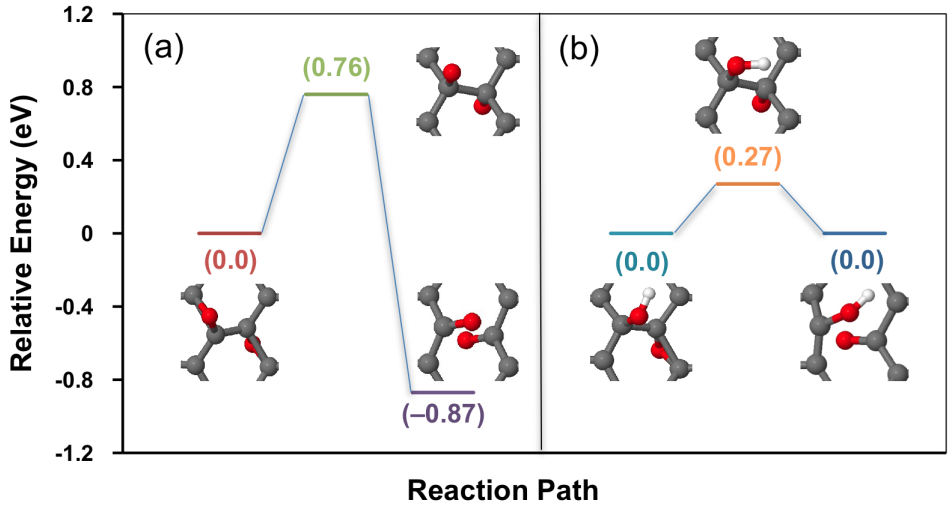

Figure 2.15: Energy barriers and transition states for the formation of (a) a carbonyl pair from a pair of epoxies and (b) a phenol-carbonyl pair from a hydroxyl and epoxy groups. The transition states in both cases are characterized by "atop" oxygen atoms on the basal plane.

A distinct mechanism for in- plane incorporation of oxygen has been observed. Loss of CO and CO_2 accompanied by the generation of carbon vacancies allows incorporation of oxygen into the basal plane. The initial configurations and the key events that lead to oxygen incorporation in the basal plane are shown in Figures 2.16 and 2.17. In the initial configuration shown in Figure 2.16a, the interactions between hydroxyls and epoxides lead to the creation of a pyran. For the initial configuration shown in Figure 2.17a, pyrans are created by interaction of epoxides in close proximity. Also, while CO_2 is formed as a byproduct in the former case (mechanism shown in Figure 2.16), CO is formed in the latter case (Figure 2.17). The individual bond-breaking and bond-formation events that lead to the incorporation of the oxygen atoms in the basal plane and the production of the CO and CO_2 molecules is presented in the Figures 2.16 and 2.17. Here, we note that the key steps in these reactions involve 1) formation of the carbonyl groups, 2) transfer or hopping of hydrogen atoms between different hydroxyl and carbonyl groups and 3) formation of new bonds between oxygen atoms that are part of carbonyl groups and under-coordinated carbon atoms in the basal plane.

Carbon vacancy generation requires higher barrier energy in comparison to carbonyl formation and hence it occurs at higher temperatures. Evidence of this is the presence of larger amounts (18%) of residual furans and pyrans for low oxygen contents (16.6%-20%) after annealing at 3000K (not shown), as compared to ~ 1-2% and <1% for 1500 K and 1000K, respectively (Figure 2.4a,b). In the case of 33% initial oxygen concentration, 60% epoxy and annealing at 1600K, highly distorted honeycomb lattice was observed due to the evolution of ~ 2% of carbon atoms. This leads to the formation of carbon

pentagon rings as well as ether rings. In such cases, the overall concentration of remaining oxygen was found to have 10% ether rings and 55% carbonyl groups.

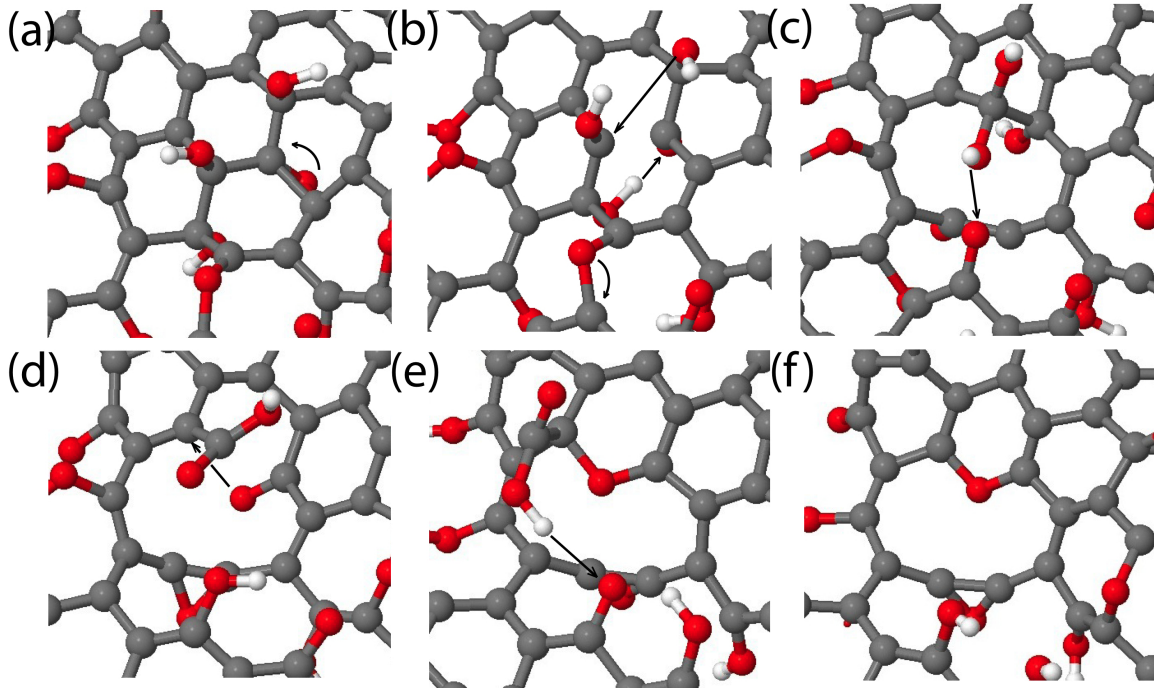

Figure 2.16: (a) Initial configuration with hydroxyl and epoxies that leads to the incorporation of an oxygen atoms in the basal plane (f). The ephemeral intermediate configurations seen in the MD simulations are shown in panels (b-e). The sequence of events resulting in the incorporation of the oxygen molecule in the basal plane are: 1) Formation of a carbonyl –phenol hole (b), 2) Transfer of hydrogen via hydrogen bonding (b-c), 3) Formation of carboxyl group (d) Hydrogen migration and release of CO_2 (e-f).

Based on our MD simulations, it can be summarized that hydroxyls desorb at low annealing temperatures, leaving the graphitized lattice intact. The epoxides require higher energy for desorption and thus are likely to remain if isolated, even for annealing at moderate temperatures. Interplay between epoxides and hydroxyls leads to incorporation of oxygen in plane as ether groups or out of plane as carbonyl groups. Also, an increase in the annealing temperature does not lead to an enhancement in the rate of oxygen

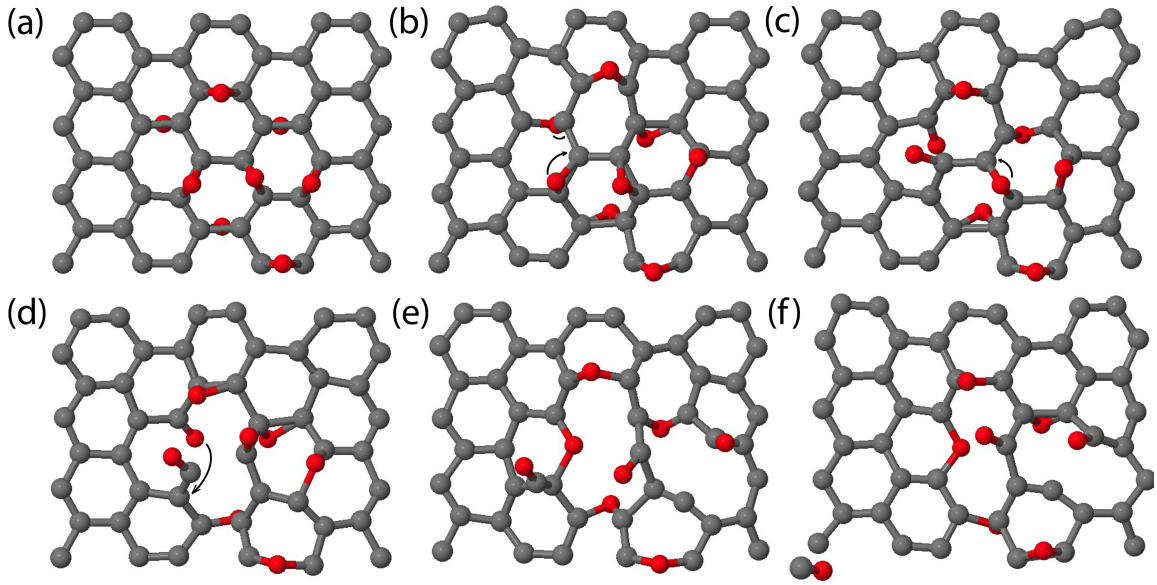

Figure 2.17: (a) Initial configuration with epoxies only that leads to the incorporation of oxygen atom in the basal plane (f). A CO molecule is produced as a byproduct of this reaction (refer panel (e)). The ephemeral intermediate configurations that facilitate the formation this molecule and the pyran configuration are indicated in panels (b-e). The sequence of events shown in this figure are: 1) breaking the C-O bonds shown arrows in (b) leading to the creation of a hole decorated by carbonyl pair shown in (c). 2) formation of an atop C-atom leading to C-C bond breaking and creation of an out-of-plane C=O configuration as shown in (d). 3) connection of the oxygen which is part of carbonyl to the under-coordinated carbon atom in (e) resulting in the formation of a CO molecule as shown in (f).

release. On the contrary, at high annealing temperatures, the probability of oxygen incorporation, as stable carbonyl groups and ether rings was found to be higher. This is consistent with our recent experimental results [56] that indicated that the rate of oxygen removal above 723K decreased substantially, reaching an almost constant value versus exponential decrease between 723 – 1373K. Thus, from our calculations, it is clear that high temperature annealing does not always lead to oxygen desorption. Incorporation of oxygen into the basal plane, in thermodynamically stable configurations such as carbonyl and ether groups hinders the possibility of complete regraphitization**.**

In light of the MD simulation results, we monitored the presence and evolution of oxygen species in GO using infrared absorption (IR) spectroscopy. The GO thin films utilized for IR and XPS analysis in this work are identical to those analyzed in detail in [8]. Each IR spectrum (i-iii) was measured at 333K, after a thermal treatment lasting 5 minutes as indicated in Figure 2.18a and its caption. The initial absorbance spectrum (spectrum i) is obtained after a mild anneal (423K) to remove solvents and physisorbed species (e.g. H_2O). The two areas highlighted in yellow indicate a spectral region that is uncertain due to changes in the SiO_2 substrate (spectrum iv) onto which the GO was deposited. After this mild anneal (423K), the pristine GO is composed of hydroxyls (broad peak at 3050-3800 cm^{-1}), carbonyls (1750–1850 cm^{-1}), carboxyls (1650-1750 cm^{-1}) [[69, 70, 98]], C=C (1500-1600 cm^{-1}), and epoxides and/or ethers (1280–1000 cm^{-1}). After annealing to 448K for 5 minutes, the differential spectrum (ii) in Figure 2.18a indicates that the carboxyl groups (from sample preparation and/or edge termination) are removed. Importantly, the intensities of the bands assigned to epoxides and hydroxyls weaken substantially. Correspondingly, close examination of the intensity of the carbonyl modes at ~1800 cm^{-1} indicates that it appears to increase. The horizontal dotted lines show the baseline in the differential spectra (i) in Figure 2.18a, so that the positive band corresponding to the formation of carbonyl groups at 423K can be clearly seen. Indeed, the formation of carbonyls is clearly seen as positive contribution within a large temperature range. The loss of epoxide and carboxyls could be observed at this temperature range as well. Experimental observations are therefore consistent with the mechanism proposed from the calculations. At higher temperatures (from 448K up to 1023K, shown in spectrum iii),

hydroxyls continuously disappear and some ether groups are formed. Hydroxyls are not detected in IR at temperatures above 773 K.

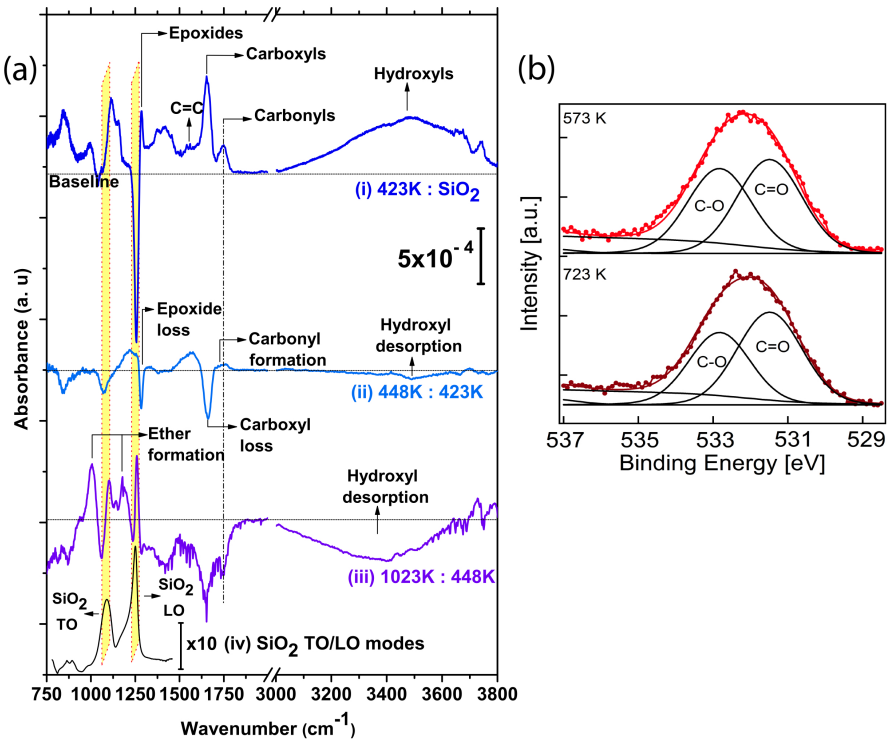

Figure 2.18: I*n-situ* transmission infrared and XPS spectra of GO: (a) (i) Absorbance spectrum of single-layer GO after annealing at 423 K, referenced to the bare oxidized silicon substrate, showing hydroxyls (broad peak at 3050-3800 cm^{-1}), carbonyls (1750-1850 cm^{-1}), carboxyls (1650-1750 cm^{-1}), C=C (1500-1600 cm^{-1}), and epoxides and/or ethers (1280–1000cm^{-1}). (ii) Differential spectrum after annealing to 448 K referenced to spectrum (i), indicating epoxide loss, carbonyl formation and hydroxyl desorption. (iii) Differential spectrum after annealing to 1023 K referenced to spectrum at 448 K anneal, showing ether formation (1000-1060 cm^{-1} and 1080-1240 cm^{-1}) and hydroxyl desorption. (iv) Absorbance spectrum (referenced to H-terminated Si), showing the full SiO_2 absorption of the oxide (750-1500 cm^{-1} range), characterized by longitudinal optical (LO, 1250 cm^{-1}) and transverse optical (TO, 1060 cm^{-1}) vibrational modes. (b) O1s XPS spectra collected on one layered GO thin film deposited on Au (10nm)/SiO_2(300nm)/Si and annealed in UHV at the indicated temperatures for 15 min. By deconvolving, the O 1s peaks collected after heating at 573 K and 723 K, two component have been identified as C-O bonds (533 eV) and C=O (531.2 eV) [74, 99] bonds. It has been found that 50% of the oxygen atoms are in C=O configurations.

The energy mode found from MD simulations for ether functional groups was compatible with substitutional oxygen in hexagonal and pentagonal rings, consistent with structures such as pyrans and furans, respectively. While it is not possible to isolate the contributions from these species in the IR spectra, the broad intensity increase between 1000 and 1280 cm^{-1} is consistent with the formation of pyrans and furans. After high temperature annealing at 1023K, residual oxygen is observed in the form of ether groups (1000-1060 cm^{-1} and 1080-1240 cm^{-1}), as suggested from MD simulations. This ether group region is difficult to analyze because of the interference caused by changes in the LO (1250 cm^{-1}) and TO (1060 cm^{-1}) modes of the SiO_2 substrate, where the peaks of GO ether groups are located.

The amount of oxygen forming double bonds to carbon estimated by XPS is also compatible with amount predicted by MD simulations**.** By deconvolving the O1s peak (Figure 2.18b), collected from single layered GO thin film after heating at 573 K and 723 K, it has been found that 50% of the oxygen is incorporated as C=O. This concentration is higher than what is expected for carbonyls and carboxyls present only at the edges of GO sheets. Excluding contamination, as the annealing has been performed in UHV (10^{-10} mbar of pressure) and the fact that FTIR clearly shows complete desorption of acetone and H_2O below 423 K, carbonyls formation is likely to be consistent with MD simulation observations (Figure 2.4a) described above which indicate an average carbonyl concentration of 45% after annealing at 1500-1600K. Carbonyls and hydroxyls in the form of ketone and phenol groups have also been observed in NMR studies reported by Szabo et al. [50], providing further confirmation of our theoretical predictions.

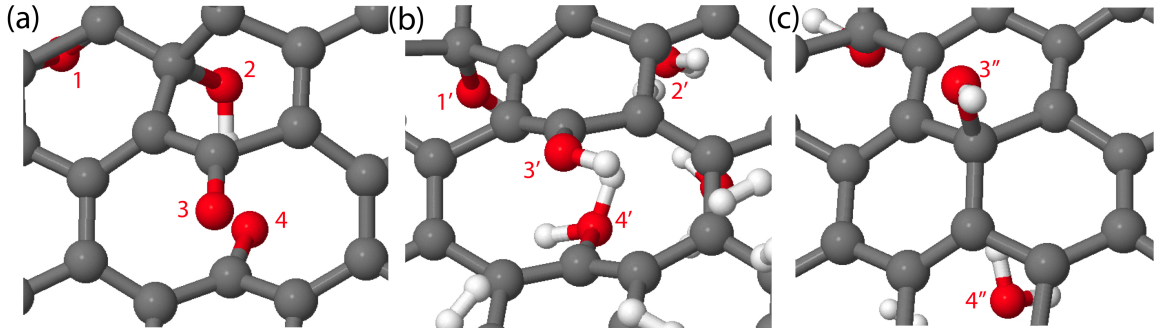

Figure 2.19: Evolution of residual oxygen groups during annealing of reduced GO in hydrogen atmosphere. (i) The epoxy group labeled 1 in (a) evolves to a hydroxyl group (1') in (b). (ii) The hydroxyl group labeled 2 leaves the basal plane in the form of a water molecule (2'). (iii) The carbonyl labeled 3 in (a) is converted to a hydroxyl (3'). (iv) The carbonyl labeled (4) leaves the basal plane in the form of a water molecule (4') leading of the healing of the hole and the restoration of sp^2 bonding in the basal plane.

Based on our detailed calculations, several pathways for more efficient reduction of graphene oxide to limit the formation of carbonyl and ether groups can be suggested. The calculations clearly point to the highly strained epoxy groups as the primary cause for the evolution of CO and CO_2, leading to holes and the formation of stable planar residual oxygen in reduced GO. Therefore if the concentration of epoxy groups in as-synthesized GO can be reduced in favor of hydroxyl groups, then evolution of oxygen during reduction can occur with minimal perturbation to the graphene basal plane. Specifically, we have found that more efficient reduction along with healing of the reduced graphene oxide can be achieved via hydrogen treatment. From the data in Table 2.1, it can be seen that the oxygen concentration can be decreased even further by reheating the reduced GO up to 1000 and 1500K in a hydrogen atmosphere (see Methods). There are three mechanisms for the enhancement in reduction using hydrogen, as indicated in Figure 2.19. The first is the evolution of residual cabonyl pairs via the formation of water

molecules and hydroxyl groups and rearrangement of the carbon atoms in the graphene sp^2 configuration leading to the healing of holes formed by the carbonyl pair (see Figure 2.19a-c). The second is the formation of hydroxyl groups with residual ether and epoxy groups in the presence of hydrogen atmosphere (see Figure 2.19b) and the subsequent evolution of the hydroxyl functional groups by thermal annealing without introducing additional defects. Finally residual hydroxyl groups are released from the basal plane by formation of water molecules (Figure 2.19b). The structure of rGO annealed in hydrogen atmosphere is shown in Figure 2.20. Although annealing as-synthesized GO in hydrogen atmosphere has been shown to yield mixed results [51, 100, 101], reheating reduced GO in hydrogen has not been reported in the literature to the best of our knowledge. The insight gained from our theoretical work suggests that the opto-electronic properties of reduced graphene oxide can be significantly improved with careful design of the reduction treatment.

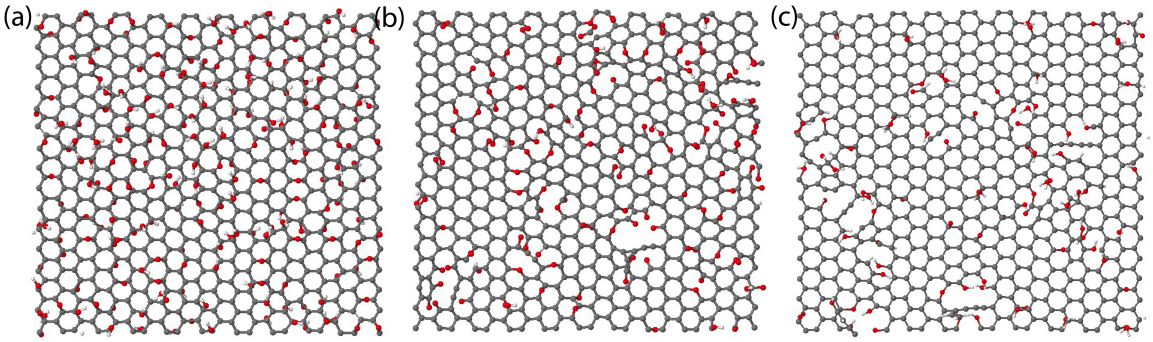

Figure 2.20: Improvement in reduction efficiency upon annealing of reduced GO in a hydrogen atmosphere. (a) Initial configuration before with hydroxyl to epoxy ratio of 3:2 at 300 K (b) structure after annealing at 1500 K (c) structure after annealing the reduced configuration from (b) in hydrogen.

Finally, in addition to clarifying the nature of residual functional groups, we also observe the formation of stable linear chains of sp-bonded carbon atoms in the simulated reduced GO structure (see Figure 2.2b). These carbon linear chains have been experimentally obtained via chemical route [102] as well as by high-temperature and high-pressure treatment [103]. Additionally, their formation and stability has been predicted by DFT simulations [104] of heating pristine nanoflakes of graphene at high temperatures. Very recently, stable and rigid carbon atomic chains were experimentally realized by removing carbon atoms row by row from graphene through the controlled energetic electron irradiation inside a transmission electron microscope [105]. The observation that carbon linear chains are formed during the deoxygenation of GO is interesting and could be a route for accessing their fundamental properties using the graphene sheet as a parent phase. In addition to the chains, other interesting features such as triangular and pentagonal arrangements of purely carbon atoms have been observed (Figure 2.2h,i).

2.4 Summary of the chapter

In summary, we report a molecular dynamics study of the evolution of graphene oxide structure upon thermal annealing. Our results provide insight into the fundamental problem limiting the device performance of GO, the nature of persistent residual oxygen that remains in GO despite aggressive chemical and thermal treatments. The MD simulations clearly reveal the formation of carbonyl and ether groups via transformation of the initial hydroxyl and epoxy groups during thermal annealing. The calculations reveal that hydroxyl groups desorb at low temperatures without altering the graphene

basal plane. Isolated epoxy groups are relatively more stable but substantially distort the graphene lattice upon desorption. The simulations indicate that removal of carbon from the graphene plane is more likely to occur when the initial hydroxyl and epoxy groups are in close proximity to each other. The reaction pathway during thermal annealing between two nearby functional groups leads to the formation of carbonyl and ether groups, which are thermodynamically very stable. The theoretical results are corroborated by FTIR and XPS experimental results. There is very good agreement between the calculations and experimental results. Our analysis suggests that careful reduction processes must be designed if highly ordered ("graphitized") graphene is to be achieved from graphene oxide.

Chapter 3

Thermal transport across twin grain boundaries in polycrystalline graphene

3.1 Introduction

The continuing demand for integration and micro-minimization is pushing the evolution of material science and technology. With the development of improved synthesis and fabrication technologies, the characteristic lengths of electronic and mechanical devices are approaching nanometer scales, which increase the power dissipation per unit area. While copper has a thermal conductivity of ~ 400 W/mK, the thermal conductivity of copper thin film, which is currently used as electrical interconnects, is below 250 W/mK [106]. Since the reliability and speed of the electromechanical devices strongly depend on temperature, materials with high thermal conductivity are in demand to spread the heat generated in such devices and scientific understanding of nanoscale thermal transport mechanism can help improve thermal management. Because of the covalent bonding between carbon atoms, which results in a large contribution of phonons in thermal transport, the allotropes of carbon such as diamond, graphite, carbon nanotubes and graphene have very high thermal conductivity. This makes them ideal for high speed

electromechanical devices and; therefore, it is important to understand the heat transport and dissipation in such materials.

Due to its high mobility, graphene has been proposed to show great promise for high speed switching in microwave and terahertz devices [107-109] and terahertz plasmon amplification [110]. Graphene exhibits exceptional electronic, thermal, optical and mechanical properties [3, 111]. Growing large-area, single-layer graphene sheets, however, remains a major challenge. Recently, a chemical vapor deposition (CVD) technique has been devised that exploits the low solubility of carbon in metals such as nickel [32, 33] and copper [34, 35] in order to grow graphene on metal foils. A consequence of this technique is that the large-area graphene sheets typically contain grain boundaries, because each grain in the metallic foil serves as a nucleation site for individual grains of graphene [34]. Thus in applications that employ large area CVD-grown graphene, the effect of grain boundaries on the fundamental physical properties must be understood.

The structures of grain boundaries in graphene have recently been studied both theoretically [112-115] and experimentally [116, 117]. The influence of grain boundaries on the electronic [112] and mechanical [115] properties of graphene has also been considered. However, to date, there are no studies that consider the role of grain boundaries on the thermal conductivity of polycrystalline graphene. Some experimental and theoretical studies have been done to measure or predict thermal conductivity of small scale structures; however, the contribution of individual defects such as impurities, grain boundaries, etc., still remains unclear. Therefore, molecular dynamics (MD) simulation method can provide an alternative technique to calculate thermal conductivity

and to understand effect of individual defects. In this chapter[1], we study heat transport across tilt grain boundaries in graphene using molecular dynamics simulations. We observe a sharp jump in the temperature across the grain boundary that is typical of an interface between regions with differing thermal properties. By relating the jump in temperature to the heat flux, we are able to extract the thermal boundary resistance (also called Kapitza resistance [119, 120]) of the grain boundaries.

3.2 Computational method

In this work, we compute the thermal conductivity using the reverse non-equilibrium molecular dynamics (RNEMD) simulations [121, 122]. The idea of the method is to impose a heat flux through the structure under study and to determine the temperature gradient that develops as a consequence of the imposed flux. As shown in Figure 3.1, the heat flux is introduced by continuously transferring energy from a "cold" slab, located at the ends of the simulation cell, to the "hot" slab, located at the middle of simulation cell.

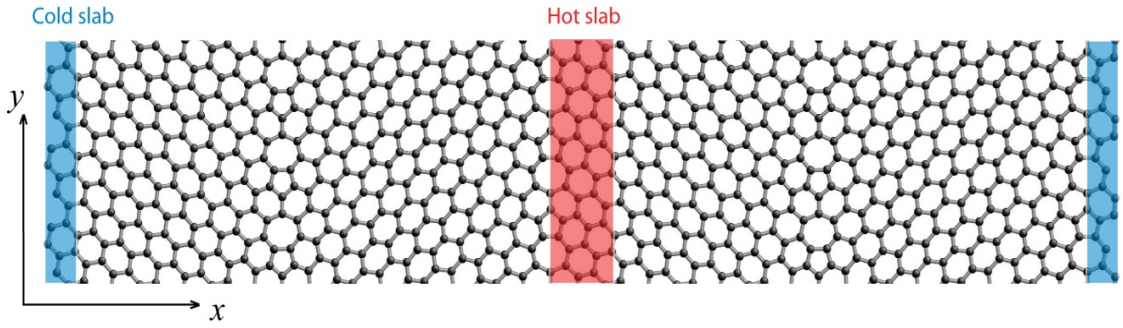

Figure 3.1: Geometry of the RNEMD simulation box. The cold slabs are placed at the ends of the simulation cell, while the hot slab is located in the middle of the cell.

---

[1] Most of the parts of this chapter are published in 118. Bagri, A., et al., *Thermal transport across Twin Grain Boundaries in Polycrystalline Graphene from Nonequilibrium Molecular Dynamics Simulations*. Nano Letters, 2011. **11**(9): p. 3917-3921.

This is accomplished by exchanging the velocities of the hottest atom in the cold slab with the coldest atom in the hot slab. The heat flux from the cold region to the hot region due to the exchange of the atoms is given by

$$q = \frac{1}{2tA_{yz}} \sum_{transfer} \frac{m}{2}(v_{hot}^2 - v_{cold}^2), \tag{3.1}$$

where q is the heat flux, t is the total time over which the simulations are carried out, A_{yz} is the cross-sectional area perpendicular to the direction of heat flow, m is the mass of the atoms, v_{hot} and v_{cold} are the velocities of the hottest atom of the cold region and the coldest atom of the hot region, respectively. The factor 2 in the denominator arises because of the periodicity of the system. When the heat flow in the structure reaches the steady state regime, averaging over the heat flux and temperature gradient and using the Fourier's heat conduction equation, the thermal conductivity can be obtained from

$$< q >= k < \frac{dT}{dx} > \tag{3.2}$$

in which k is the thermal conductivity and T is the temperature. The brackets, <>, indicate the average of the quantities over time as well as over the particles in the simulation cell. The above approach for computing the thermal conductivity of a homogenous system can also be generalized to the case of a system with defects. In the case of grain boundaries we consider here, imposing a heat flux leads to a "jump" in temperature across the boundary. The jump gives a measure of the boundary conductance (Kapitza conductance) G of the grain boundary through the relation [123]

$$G = \frac{< q >}{\Delta T} \tag{3.3}$$

Furthermore, the temperature profiles that develop across the grains can be analyzed to obtain their thermal conductivity as a function of their orientation.

The structures of tilt grain boundaries in zigzag-oriented graphene are shown in Figure 3.2 for different grain boundary angles. The grain boundaries consist of repeating five- and seven-membered ring pairs (5-7 pairs) that are separated by several hexagonal rings (hex rings). As the grain boundary angle increases, the number of hex rings separating the 5-7 defects decreases, with the ultimate limit occurring at 21.7° when only a single hex ring separates the periodic 5-7 defects. Therefore, more severe grain boundary angles are composed of higher defect densities. The repeating defect pairs can also be thought of as an array of edge dislocations with horizontal Burgers vectors where the five-membered rings represent the extra plane of atoms. In our simulations, periodic boundary conditions are employed both along the direction of heat flow (x) and perpendicular to the direction of heat flow (y). The atomic interactions are defined by a modified version of the Tersoff potential [124] which has been recently shown to yield values of the acoustic-phonon velocities that are in excellent agreement with measured data. The potential also provides lattice thermal conductivity values in single-walled carbon nanotubes and graphene that are considerably improved compared to those obtained from the original parameter sets [125, 126]. The atomic coordinates and the overall periodic dimensions of the simulation cell is first optimized using the gradient-based minimization method implemented in the Large-Scale Atomic/Molecular Massively Parallel Simulation (LAMMPS) molecular dynamics package [127] in a microcanonical NVE ensemble until

the forces on atoms are less than 10^{-8} eV/Å. RNEMD simulations are then carried out on the relaxed structure at room temperature with a time step of 0.5 fs. Before the temperature profiles are computed to infer thermal conductivity, the system is allowed to evolve for 44,000,000 MD steps during which the velocities of the atoms in the hot and cold region are exchanged every 100 MD time steps. After reaching the steady state regime, the temperature gradient through the structure is obtained by averaging over 8,000,000 MD steps. The temperature profiles are determined by dividing the structure into slabs that are approximately 10Å wide.

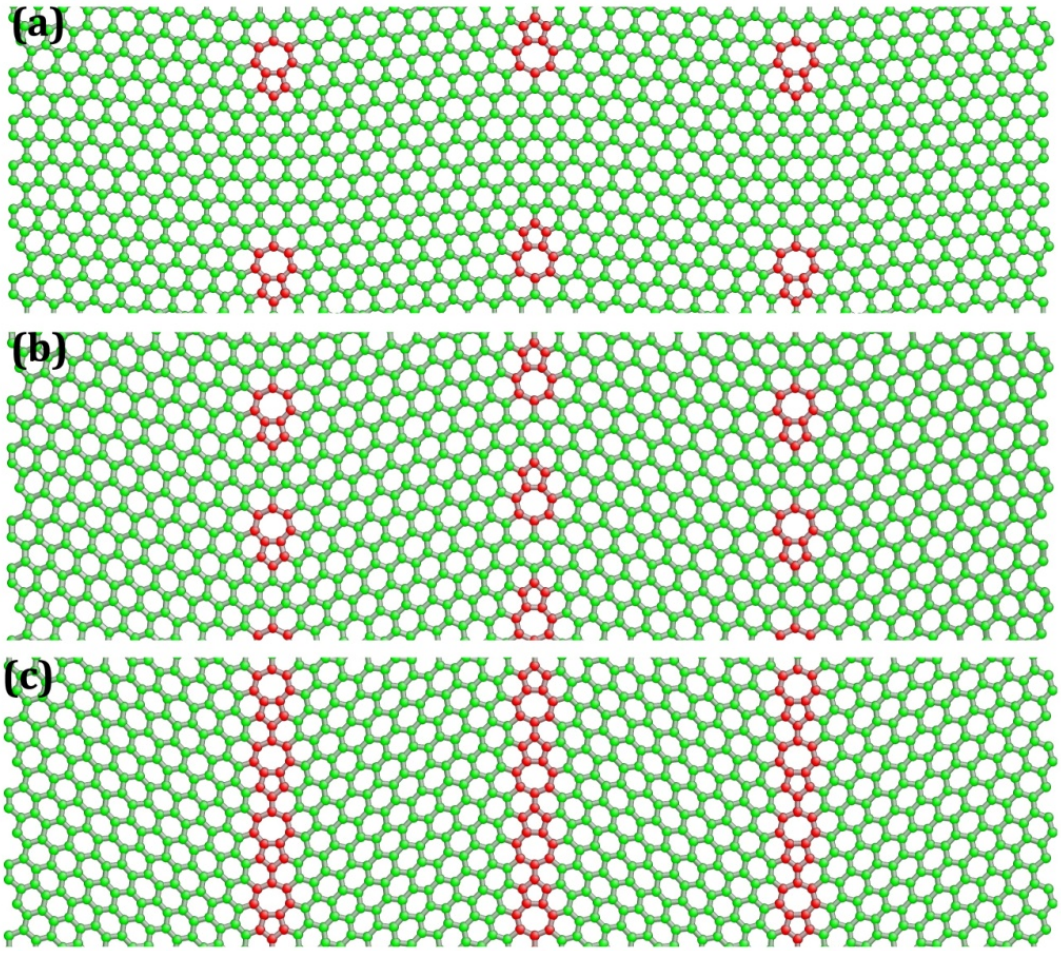

Figure 3.2: Structure of tilt grain boundaries with misorientation angles of (a) 5.5 (b) 13.2 and (c) 21.7 degree.

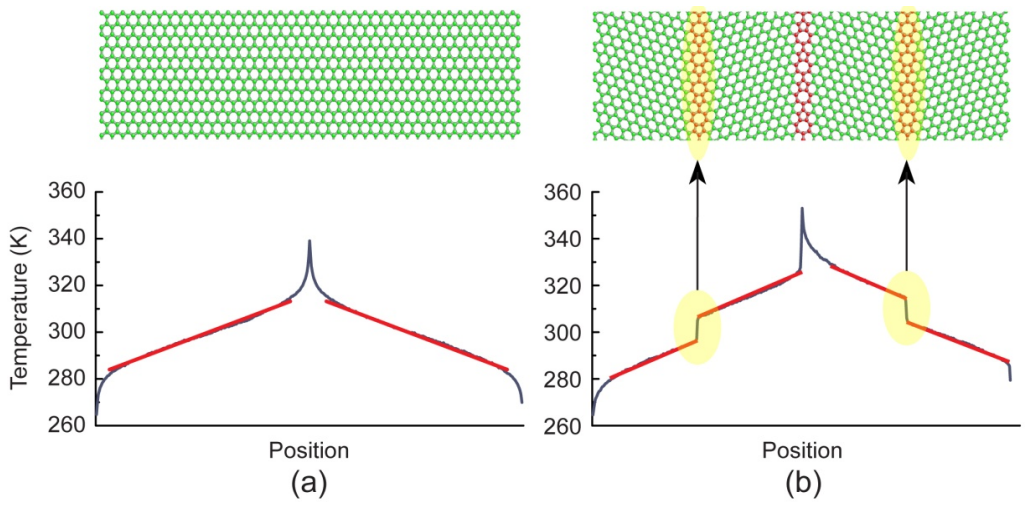

Figure 3.3: Typical temperature profile through the geometry of (a) graphene and (b) graphene with grain boundaries obtained by using the RNEMD method.

3.3 Results and discussion

First, we validate our approach by computing the thermal conductivity of defect-free graphene. The temperature variation obtained in our calculations in this case is shown in Figure 3.3a. The temperature profile is nonlinear near the hot and cold ends due to finite size effects as noted in previous work [128] and the high thermal conductivity of graphene. Similar temperature profiles have also been noted in carbon nanotubes (CNTs) [129]. Care must be taken in the extraction of thermal conductivity from this nonlinear profile, which indicates that thermal transport is not fully diffusive. To obtain the correct diffusive thermal conductivity [129] we take the temperature gradient of the middle portion between the thermostats to avoid edge effects. Even with this correction, the thermal conductivity inferred from NEMD calculations depends on the size of the system. We find that the conductivity of cells with periodic lengths of 50nm, 100nm, and

250nm, are 532, 898, and 1460 W/mK, respectively. To calculate the thermal conductivity of 2-D graphene sheets, the cross-sectional area is defined as $A_{yz}=wd$, where w is the width of the sheet and d is the thickness (chosen as the interplanar distance in graphite =3.35 Å). The dependence of the thermal conductivity on the length of the simulation cell can be understood by noting that the mean free path of phonons in graphene is of the order of 775nm [130], which is bigger than the size of our simulation cells. Therefore, in addition to phonon-phonon scattering, scattering at the heat baths (or boundaries) of the system must be considered. Based on the kinetic theory of phonon transport [131], the thermal conductivity is proportional to the mean free path for phonon scattering. In the case where phonons scatter at the heat reservoir, the effective mean free path is given by

$$\frac{1}{l_{eff}} = \frac{1}{l_{ph-ph}} + \frac{1}{l_g}, \tag{3.4}$$

where $l_{ph\text{-}ph}$ denotes phonon-phonon scattering length and l_g is scattering length due to the boundaries in a finite system and can be approximated to be the length of the simulation box. Based on this relation, the thermal conductivity satisfies the relation

$$\frac{1}{k} \propto \frac{1}{l_g} + \frac{1}{l_{ph-ph}}, \tag{3.5}$$

which implies that a plot of the inverse of thermal conductivity, k, versus the inverse of the system size l_g, should be a linear curve, the intercept being the thermal conductivity of the infinitely large system. Indeed, the plot of the inverse of the thermal conductivity as a function of the size of the system in Figure 3.4 confirms this scaling relation. The scaling approach we use here has also been used in earlier work on 3D systems [128,

132]. From the intercepts of the plot in Figure 3.4, we find the thermal conductivity of defect-free graphene along the zig-zag direction to be 2650 W/mK. This result is in excellent agreement with the result (2600 W/mK) obtained using the same potential we use here, but a different approach, namely the non-equilibrium molecular dynamics (NEMD) method [126]. Furthermore, our results agree with the theoretical [133, 134] and experimental [12, 135] values, which lie in the range 2000-5000 W/mK. Our results for the thermal conductivity of finite-sized graphene also agree with the results reported in Ref. ([136]), where NEMD has been used and the thermal conductivity of graphene of length 29.5nm was found to be 256 W/mK.

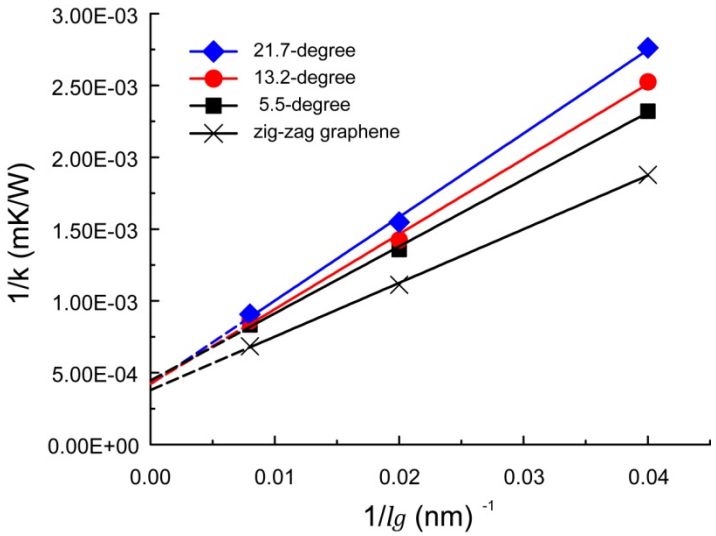

Figure 3.4: Inverse of thermal conductivity for zigzag-oriented graphene as a function of grain orientation versus the inverse of grain size (l_g). The intercepts for the case of zig-zag graphene, 5.5, 13.2, and 21.7 degree oriented grains are $37x10^{-5}$, $45\ x10^{-5}$, $42\ x10^{-5}$ and $42\ x10^{-5}$, respectively.

Next, we consider the temperature profile in the case of graphene with tilt grain boundaries (Figure 3.3b). We find a nearly linear temperature profile in the grains, but observe a jump in the temperature at the grain boundaries. A plot of the thermal

conductivity of grains (inferred from the slope of the linear part of the temperature profile) of different orientations as a function of size is plotted in Figure 3.5. As in the case of zigzag oriented grains, the inverse of the thermal conductivity decreases linearly with the size of the simulation cell. The intercepts of the curves in Figure 3.4 show that thermal conductivity is anisotropic, but only weakly depends on the orientation of the grains (k= 2220, 2380, 2380 W/mK for 5.5, 13.2, and 21.7 degree grains, respectively).

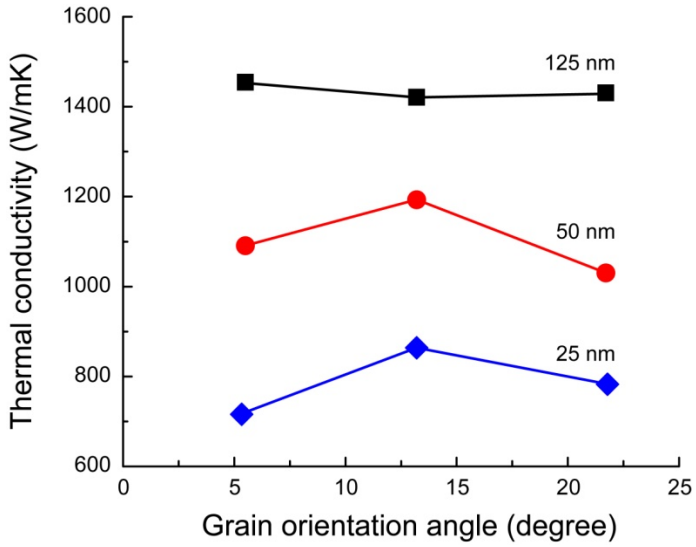

Figure 3.5: Thermal conductivity of graphene grains of different sizes (25, 50, and 125 nm) versus the orientation of the grain.

The jump in the temperature across the grain boundary can be used in Equation 3.3 to obtain the boundary conductance of the grain boundaries. A summary of these temperature jumps as a function of the grain sizes and angles is given in Table 3.1. Using the measured jumps, we find that the boundary conductance for the grain boundaries we have considered fall in the range $1.5\text{x}10^{10}$-$4.5\text{x}10^{10}$ W/m^{2}K (refer to Figure 3.6). These values are 6-to-12, 10-to-50, and 6-to-30 times larger than the boundary conductance's reported for grain boundaries in ultra-nano-crystalline diamond thin films with grain

boundaries on the (001) plane [137], silicon-silicon (001) ∑29 grain boundaries [123, 138], and the Si-Ge interface with the <100> orientation [139], respectively. Note that the boundary conductance decreases with increasing the misorientation angle of the grain boundaries. This can be qualitatively understood by considering the defect density as a function of grain boundary angle – the higher the misorientation angle the larger is the density of 5-7 defect pairs per unit length of the boundary, which can lead to increase of scattering of phonons and hence a drop in the boundary conductance. We also observe that computed conductance depends slightly on the size of the grains. A similar dependence of the boundary conductance on size has also been reported in Refs. ([123]) and ([139]) for Si-Ge and silicon grain boundaries. This has been attributed to scattering of long wavelength phonons at the heat reservoirs and at the boundaries [131, 140], but a scaling of the conductance with length has not been provided.

Table 3.1: Temperature jumps at the grain boundaries and heat flux (given in parentheses) for different grain sizes and angles. Units for the given temperature and heat flux values are Kelvin and Watt per square meter, respectively.

Grain orientation angle (degree)	Grain size (nm)		
	25	50	125
5.5	8.13 (1.95×10^{11})	6.18 (1.89×10^{11})	4.40 (1.89×10^{11})
13.2	12.17 (2.15×10^{11})	8.97 (2.13×10^{11})	7.36 (2.19×10^{11})
21.7	12.98 (2.12×10^{11})	10.24 (2.21×10^{11})	7.63 (2.13×10^{11})

Note that when grains are very large in size, the scattering of phonons within the grains will primarily determine the thermal conductivity of the polycrystalline graphene, but with decreasing grain size the contribution to thermal conductivity due to scattering from

grain boundaries will become more significant. For the polycrystalline graphene sheet in Figure 3.2 with grain spacing l_g, the thermal conductivity k_p can be written as

$$k_p^{-1} = k_g^{-1} + \left(l_g G\right)^{-1}, \tag{3.6}$$

where k_g is the thermal conductivity of the grain. Using this expression and the computed values of boundary conductance for the tilt boundaries, we can now estimate the critical size of grains below which the contribution from the grain boundaries becomes comparable to the scattering from the grains. This length scale is simply the ratio of the thermal conductivity to the boundary conductance. For the tilt boundaries considered here, this length scale is of the order of 0.1 microns. While a systematic study of the scaling of the thermal conductivity of polycrystalline graphene as a function of grain size has not been reported, the thermal conductivity of exfoliated graphene [141] is generally observed to be higher than the thermal conductivity of CVD-graphene [12]. Experiments on graphene with well controlled grain sizes and orientations can help verify the predictions of this study, namely, the scaling of the boundary conductance (Equation 3.6) and the computed value of boundary conductance as a function of the grain boundary angle. The former can be studied by measuring the overall thermal conductivity of polycrystalline graphene for different grain sizes, while the latter will involve measurement of temperature drop across individual boundaries (once they have been identified using appropriate microscopy techniques).

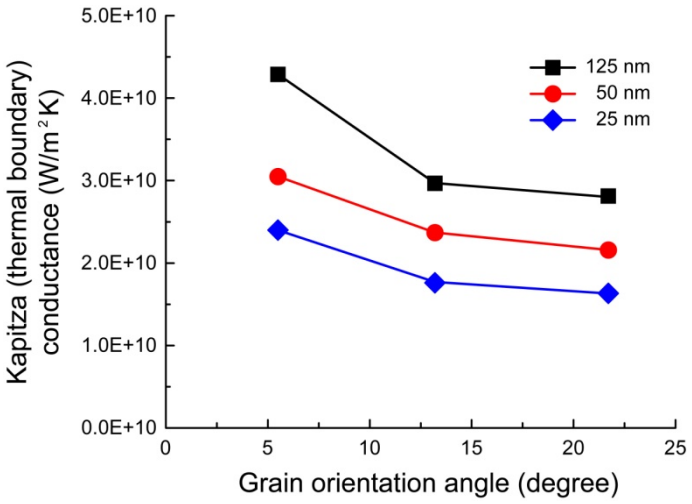

Figure 3.6: Boundary conductance of grain boundaries as a function of orientation. The curves are labeled by the size of the grains used to compute the boundary conductance.

2.4 Summary of the chapter

In summary we have studied thermal transport across tilt grain boundaries in polycrystalline graphene. As in the case of interfaces in the dissimilar materials, we find a jump in temperature at grain boundary when a constant heat flux is applied. We have used this information to extract the boundary conductance, which lies in the range of $1.5x10^{10}$-$4.5x10^{10}$ W/m^2K in the case of tilt grain boundaries. Based on this information, we have identified a critical grain size of about 0.1 microns below which the contribution of tilt boundaries becomes comparable to that of the contribution from the grains themselves. We also note that here we have considered the most common type of tilt boundaries reported in the literature [112-115]; future work on thermal conductance of other types of grain boundaries can shed further light on the thermal transport properties of polycrystalline graphene. Recent experiments have shown that defects such as vacancies and voids tend to segregate at grain boundaries [116, 117]. These defects can

be expected to further lower the thermal conductance of the boundaries. We hope to consider the effect of these defects in forthcoming publications.

Chapter 4

Concluding remarks

Having deep knowledge of nature of materials and their properties is crucial to guide the experiments and make new devices. In this regard and to reduce the costs of experiments, researchers have tried to use analytical and numerical tools in modeling and simulation of the processes and calculation of the material properties. In this thesis, the combinations of atomistic simulations and experimental measurements have been used to elucidate the atomic evolution of graphene oxide structure during thermal reduction process. We also have used molecular dynamics simulations to calculate the thermal conductance across boundaries of polycrystalline graphene and analyzed the effect of size and orientation of the grains. The main conclusions of this work are as follows

Structural evolution of graphene oxide during thermal reduction process

Using MD and DFT calculations in conjunction with experimental measurements the following results have been revealed about the atomic details of reduced graphene oxide.

1) Transformation of the initial hydroxyl and epoxy groups during thermal annealing can lead to formation of carbonyl and ether groups.

2) Hydroxyl groups desorb at low temperatures without altering the graphene basal plane.
3) Isolated epoxy groups are relatively more stable but substantially distort the graphene lattice upon desorption.
4) The simulations indicate that thermal reduction may result in removal of carbon from the graphene plane when the initial hydroxyl and epoxy groups are in close proximity to each other.

Our simulations suggest that careful reduction processes must be designed if highly ordered graphene is to be achieved from graphene oxide. To this end, one may consider using chemical reactants other than hydrogen gas to remove further functional groups. Also, the effects of remaining functional groups on optoelectronic and thermomechanical properties of graphene oxide must be investigated.

Thermal conductance across grain boundaries of polycrystalline graphene

We have simulated polycrystalline graphene with different size and orientation of grains and performed MD calculations to determine the thermal conductance across grain boundaries. The summary of our results is

1) We find a jump in temperature at grain boundary when a constant heat flux is applied.
2) The boundary conductance extracted from these temperature jumps lies in the range of 1.5×10^{10}-4.5×10^{10} W/m^{2}K in the case of tilt grain boundaries.

3) We have identified a critical grain size of about 0.1 microns below which the contribution of tilt boundaries becomes comparable to that of the contribution from the grains themselves
4) Results show that when the size of structure is much less than phonon mean free path both thermal conductivity and boundary thermal conductance of polycrystalline are size dependent properties.
5) MD simulations revealed that thermal conductivity of graphene is anisotropic, but only weakly depends on the orientation of the grains.

While we considered the most common type of tilt boundaries reported in the literature, future works on thermal conductance of other types of grain boundaries can shed further light on the thermal transport properties of polycrystalline graphene. Also, other type of defects such as vacancies and voids, which tend to segregate at grain boundaries, may have significant effect on thermal conductance of graphene and may be considered as future works. Further investigations for the analysis of the temperature and functional groups effects are also needed.

Bibliography

1. Novoselov, K.S., et al., *Electric field effect in atomically thin carbon films.* Science, 2004. **306**(5696): p. 666-669.
2. Novoselov, K.S., et al., *Two-dimensional gas of massless Dirac fermions in graphene.* Nature, 2005. **438**(7065): p. 197-200.
3. Geim, A.K. and K.S. Novoselov, *The rise of graphene.* Nature Materials, 2007. **6**(3): p. 183-191.
4. Acheson, E.G., *Deflocculated graphite.* Journal of the Franklin Institute, 1907. **164**: p. 0375-0382.
5. de Heer, W.A., *Epitaxial graphene: A new electronic material for the 21st century.* Mrs Bulletin, 2011. **36**(8): p. 632-639.
6. Brodie, B.C., Proceedings of the Royal Society of London, 1859. **10**: p. 249.
7. Boehm, H.P., et al., *Dunnste Kohlenstoff-Folien.* Zeitschrift Fur Naturforschung Part B-Chemie Biochemie Biophysik Biologie Und Verwandten Gebiete, 1962. **B 17**(3): p. 150-&.
8. Bolotin, K.I., et al., *Ultrahigh electron mobility in suspended graphene.* Solid State Communications, 2008. **146**(9-10): p. 351-355.
9. Castro Neto, A.H., et al., *The electronic properties of graphene.* Reviews of Modern Physics, 2009. **81**(1): p. 109-162.
10. Lee, C., et al., *Measurement of the elastic properties and intrinsic strength of monolayer graphene.* Science, 2008. **321**(5887): p. 385-388.

11. Nair, R.R., et al., *Fine structure constant defines visual transparency of graphene.* Science, 2008. **320**(5881): p. 1308-1308.

12. Cai, W.W., et al., *Thermal Transport in Suspended and Supported Monolayer Graphene Grown by Chemical Vapor Deposition.* Nano Letters, 2010. **10**(5): p. 1645-1651.

13. Berger, C., et al., *Electronic confinement and coherence in patterned epitaxial graphene.* Science, 2006. **312**(5777): p. 1191-1196.

14. Chen, J.H., et al., *Printed graphene circuits.* Advanced Materials, 2007. **19**(21): p. 3623-+.

15. Tombros, N., et al., *Electronic spin transport and spin precession in single graphene layers at room temperature.* Nature, 2007. **448**(7153): p. 571-U4.

16. Wimmer, M., et al., *Spin currents in rough graphene nanoribbons: Universal fluctuations and spin injection.* Physical Review Letters, 2008. **100**(17): p. -.

17. Bunch, J.S., et al., *Impermeable atomic membranes from graphene sheets.* Nano Letters, 2008. **8**(8): p. 2458-2462.

18. Bunch, J.S., et al., *Electromechanical resonators from graphene sheets.* Science, 2007. **315**(5811): p. 490-493.

19. Blundell, S.J. and F.L. Pratt, *Organic and molecular magnets.* Journal of Physics-Condensed Matter, 2004. **16**(24): p. R771-R828.

20. Leuenberger, M.N. and D. Loss, *Quantum computing in molecular magnets.* Nature, 2001. **410**(6830): p. 789-793.

21. Stankovich, S., et al., *Graphene-based composite materials.* Nature, 2006. **442**(7100): p. 282-286.

22. Dikin, D.A., et al., *Preparation and characterization of graphene oxide paper.* Nature, 2007. **448**(7152): p. 457-460.

23. Gilje, S., et al., *A chemical route to graphene for device applications.* Nano Letters, 2007. **7**(11): p. 3394-3398.

24. Eda, G., G. Fanchini, and M. Chhowalla, *Large-area ultrathin films of reduced graphene oxide as a transparent and flexible electronic material.* Nature Nanotechnology, 2008. **3**(5): p. 270-274.

25. Hirata, M., et al., *Thin-film particles of graphite oxide 1: High-yield synthesis and flexibility of the particles.* Carbon, 2004. **42**(14): p. 2929-2937.

26. Stankovich, S., et al., *Stable aqueous dispersions of graphitic nanoplatelets via the reduction of exfoliated graphite oxide in the presence of poly(sodium 4-styrenesulfonate).* Journal of Materials Chemistry, 2006. **16**(2): p. 155-158.

27. Gomez-Navarro, C., et al., *Electronic transport properties of individual chemically reduced graphene oxide sheets.* Nano Letters, 2007. **7**(11): p. 3499-3503.

28. Stankovich, S., et al., *Synthesis and exfoliation of isocyanate-treated graphene oxide nanoplatelets.* Carbon, 2006. **44**(15): p. 3342-3347.

29. Watcharotone, S., et al., *Graphene-silica composite thin films as transparent conductors.* Nano Letters, 2007. **7**(7): p. 1888-1892.

30. McAllister, M.J., et al., *Single sheet functionalized graphene by oxidation and thermal expansion of graphite.* Chemistry of Materials, 2007. **19**(18): p. 4396-4404.

31. Schniepp, H.C., et al., *Functionalized single graphene sheets derived from splitting graphite oxide.* Journal of Physical Chemistry B, 2006. **110**(17): p. 8535-8539.

32. Yu, Q.K., et al., *Graphene segregated on Ni surfaces and transferred to insulators.* Applied Physics Letters, 2008. **93**(11): p. 113103.

33. Kim, K.S., et al., *Large-scale pattern growth of graphene films for stretchable transparent electrodes.* Nature, 2009. **457**(7230): p. 706-710.

34. Li, X.S., et al., *Large-Area Synthesis of High-Quality and Uniform Graphene Films on Copper Foils.* Science, 2009. **324**(5932): p. 1312-1314.

35. Levendorf, M.P., et al., *Transfer-Free Batch Fabrication of Single Layer Graphene Transistors.* Nano Letters, 2009. **9**(12): p. 4479-4483.

36. Alder, B.J. and T.E. Wainwright, *Phase Transition for a Hard Sphere System.* Journal of Chemical Physics, 1957. **27**(5): p. 1208-1209.

37. Alder, B.J. and T.E. Wainwright, *Studies in Molecular Dynamics .1. General Method.* Journal of Chemical Physics, 1959. **31**(2): p. 459-466.

38. Rahman, A., *Correlations in Motion of Atoms in Liquid Argon.* Physical Review a-General Physics, 1964. **136**(2A): p. A405-&.

39. Stilling.Fh and A. Rahman, *Improved Simulation of Liquid Water by Molecular-Dynamics.* Journal of Chemical Physics, 1974. **60**(4): p. 1545-1557.

40. Daw, M.S., S.M. Foiles, and M.I. Baskes, *The Embedded-Atom Method - a Review of Theory and Applications.* Materials Science Reports, 1993. **9**(7-8): p. 251-310.

41. Cleri, F. and V. Rosato, *Tight-Binding Potentials for Transition-Metals and Alloys.* Physical Review B, 1993. **48**(1): p. 22-33.

42. Tersoff, J., *New Empirical-Approach for the Structure and Energy of Covalent Systems.* Physical Review B, 1988. **37**(12): p. 6991-7000.

43. Tersoff, J., *Modeling Solid-State Chemistry - Interatomic Potentials for Multicomponent Systems.* Physical Review B, 1989. **39**(8): p. 5566-5568.

44. Brenner, D.W., *Empirical Potential for Hydrocarbons for Use in Simulating the Chemical Vapor-Deposition of Diamond Films.* Physical Review B, 1990. **42**(15): p. 9458-9471.

45. Brenner, D.W., *Correction.* Physical Review B, 1992. **46**(3): p. 1948-1948.

46. van Duin, A.C.T., et al., *ReaxFF: A reactive force field for hydrocarbons.* J. Phys. Chem. A, 2001. **105**(41): p. 9396-9409.

47. Hohenberg, P. and W. Kohn, *Inhomogeneous Electron Gas.* Physical Review B, 1964. **136**(3B): p. B864-&.

48. Kohn, W. and L.J. Sham, *Self-Consistent Equations Including Exchange and Correlation Effects.* Physical Review, 1965. **140**(4A): p. 1133-&.

49. Sholl, D.S. and J.A. Steckel, *Density functional theory : a practical introduction*. 2009, Hoboken, N.J.: Wiley. xii, 238 p.

50. Szabó, T., et al., *Evolution of surface functional groups in a series of progressively wxidized graphite oxides.* Chem. Mater., 2006. **18**(11): p. 2740-2749.

51. Wang, X., L. Zhi, and K. Mullen, *Transparent, conductive graphene electrodes for dye-sensitized solar cells.* Nano Lett., 2007. **8**: p. 323-327.

52. Becerril, H.A., et al., *Evaluation of solution-processed reduced graphene oxide films as transparent conductors.* ACS Nano, 2008. **2**(3): p. 463-470.

53. Eda, G., G. Fanchini, and M. Chhowalla, *Large-area ultrathin films of reduced graphene oxide as a transparent and flexible electronic material.* Nature Nanotech., 2008. **3**: p. 270-274.

54. Robinson, J.T., et al., *Wafer-scale reduced graphene oxide films for nanomechanical devices.* Nano Lett., 2008. **8**(10): p. 3441-3445.

55. Eda, G., et al., *Transparent and conducting electrodes for organic electronics from reduced graphene oxide.* Appl. Phys. Lett., 2008. **92**: p. 233305.

56. Mattevi, C., et al., *Evolution of electrical, chemical, and structural properties of transparent and conducting chemically derived graphene thin films.* Adv. Funct. Mater., 2009. **19**: p. 2577-2583.

57. Jung, I., et al., *Tunable electrical conductivity of individual graphene oxide sheets reduced at "low" temperatures.* Nano Lett., 2008. **8**(12): p. 4283–4287.

58. Gómez-Navarro, C., et al., *Electronic transport properties of individual chemically reduced graphene oxide sheets.* Nano Lett., 2007. **7**(11): p. 3499-3503.

59. Neto, A.H.C., et al., *The electronic properties of graphene.* Reviews of Modern Physics, 2009. **81**(1): p. 109-162.

60. Du, X., et al., *Approaching ballistic transport in suspended graphene.* Nature Nanotech., 2008. **3**: p. 491-495.

61. Stankovich, S., et al., *Synthesis of graphene-based nanosheets via chemical reduction of exfoliated graphite oxide.* Carbon, 2007. **45**(7): p. 1558-1565.

62. Bourlinos, A.B., et al., *Graphite oxide: Chemical reduction to graphite and surface modification with primary aliphatic amines and amino acids.* Langmuir, 2003. **19**(15): p. 6050-6055.

63. Hyeon-Jin, S., et al., *Efficient reduction of graphite oxide by sodium borohydride and its effect on electrical conductance.* Adv. Funct. Mater, 2009. **19**(12): p. 1987-1992.

64. Bagri, A., et al., *Structural evolution during the reduction of chemically derived graphene oxide.* Nature Chemistry, 2010. **2**(7): p. 581-587.

65. Bagri, A., et al., *Stability and Formation Mechanisms of Carbonyl- and Hydroxyl-Decorated Holes in Graphene Oxide.* Journal of Physical Chemistry C, 2010. **114**(28): p. 12053-12061.

66. Mkhoyan, K.A., et al., *Atomic and electronic structure of graphene-oxide.* Nano Lett., 2009. **9**(3): p. 1058-1063.

67. Wilson, N.R., et al., *Graphene oxide: Structural analysis and application as a highly transparent support for electron microscopy.* ACS Nano, 2009. **3**: p. 2547-2556.

68. Lerf, A., et al., *Structure of graphite oxide revisited.* J. Phys. Chem. B, 1998. **102**(23): p. 4477-4482.

69. Szabó, T., O. Berkesi, and I. Dékány, *DRIFT study of deuterium-exchanged graphite oxide.* Carbon, 2005. **43**(15): p. 3186-3189.

70. Fuente, E., et al., *Infrared spectroscopy of carbon materials: A quantum chemical study of model compounds.* J. Phys. Chem. B, 2003. **107**(26): p. 6350-6359.

71. Nakajima, T. and Y. Matsuo, *Formation process and structure of graphite oxide.* Carbon, 1994. **32**(3): p. 469-475.

72. Ulrich, H. and H. Rudolf, *Über die säurenatur und die methylierung von graphitoxyd.* Ber. Dtsch. Chem. Ges., 1939. **72**(4): p. 754-771.

73. Scholz, W. and H.P. Boehm, *Untersuchungen am graphitoxid. VI. Betrachtungen zur struktur des graphitoxids.* Anorg. Allg. Chem., 1969. **369**(3-6): p. 327-340.

74. Hontoria-Lucas, C., et al., *Study of oxygen-containing groups in a series of graphite oxides: Physical and chemical characterization.* Carbon, 1995. **33**(11): p. 1585-1592.

75. Brodie, B.C., *On the atomic weight of graphite.* Philos. Trans. R. Soc. London, 1959. **149**: p. 249-259.

76. Staudenmaier, L., *Verfahren zur darstellung der graphitsaure.* Ber. Deut. Chem. Ges., 1898. **31**: p. 1481.

77. W. S. Hummers, J. and R.E. Offeman, *Preparation of graphitic oxide.* J. Am. Chem. Soc., 1958. **80**: p. 1339.

78. Cassagneau, T., F. Guerin, and J.H. Fendler, *Preparation and characterization of ultrathin films layer-by-layer self-assembled from graphite oxide nanoplatelets and polymers.* Langmuir, 2000. **16**(18): p. 7318-7324.

79. Szabó, T., et al., *Enhanced acidity and pH-dependent surface charge characterization of successively oxidized graphite oxides.* Carbon, 2006. **44**(3): p. 537-545.

80. Chenoweth, K., et al., *Simulations on the Thermal Decomposition of a Poly(dimethylsiloxane) Polymer Using the ReaxFF Reactive Force Field.* J. Am. Chem. Soc., 2005. **127**(19): p. 7192-7202.

81. Chenoweth, K., A.C.T. van Duin, and W.A. Goddard, *ReaxFF Reactive Force Field for Molecular Dynamics Simulations of Hydrocarbon Oxidation.* J. Phys. Chem. A, 2008. **112**(5): p. 1040-1053.

82. Kresse, G. and J. Furthmüller, *Efficient iterative schemes for ab initio total-energy calculations using a plane-wave basis set.* Phys. Rev. B, 1996. **54**(Copyright (C) 2009 The American Physical Society): p. 11169.

83. Kresse, G. and J. Furthmüller, *Efficiency of ab-initio total energy calculations for metals and semiconductors using a plane-wave basis set.* Comput. Mater. Sci., 1996. **6**(1): p. 15-50.

84. Kresse, G. and D. Joubert, *From ultrasoft pseudopotentials to the projector augmented-wave method.* Phys. Rev. B, 1999. **59**(Copyright (C) 2009 The American Physical Society): p. 1758.

85. Perdew, J.P., K. Burke, and M. Ernzerhof, *Generalized Gradient Approximation Made Simple.* Phys. Rev. Lett., 1996. **77**(Copyright (C) 2009 The American Physical Society): p. 3865.

86. Cai, W., et al., *Synthesis and solid-state NMR structural characterization of ^{13}C-labeled graphite oxide.* Science, 2008. **321**(5897): p. 1815-1817.

87. Paci, J.T., T. Belytschko, and G.C. Schatz, *Computational studies of the structure, behavior upon heating, and mechanical properties of graphite oxide.* J. Phys. Chem. C, 2007. **111**(49): p. 18099-18111.

88. Gomez-Navarro, C., et al., *Atomic Structure of Reduced Graphene Oxide.* Nano Letters, 2010. **10**(4): p. 1144-1148.

89. He, H., et al., *A new structural model for graphite oxide.* Chem. Phys. Lett., 1998. **287**(1-2): p. 53-56.

90. Szabo, T., et al., *Evolution of surface functional groups in a series of progressively oxidized graphite oxides.* Chemistry of Materials, 2006. **18**(11): p. 2740-2749.

91. Cai, W.W., et al., *Synthesis and solid-state NMR structural characterization of C-13-labeled graphite oxide.* Science, 2008. **321**(5897): p. 1815-1817.

92. Gao, W.A., Lawrence B.; Ci, Lijie Ci; and Ajayan, Pullickel M., *New insights into the structure and reduction of graphite oxide.* Nature Chemistry, 2009. **1**: p. 403-408.

93. Li, Z.Y., et al., *How Graphene Is Cut upon Oxidation?* Journal of the American Chemical Society, 2009. **131**(18): p. 6320-+.

94. Ajayan, P.M. and B.I. Yakobson, *Materials science - Oxygen breaks into carbon world.* Nature, 2006. **441**(7095): p. 818-819.

95. Li, J.L., et al., *Oxygen-driven unzipping of graphitic materials.* Physical Review Letters, 2006. **96**(17): p. -.

96. Berendsen, H.J.C., et al., *Molecular-Dynamics with Coupling to an External Bath.* Journal of Chemical Physics, 1984. **81**(8): p. 3684-3690.

97. Paci, J.T., T. Belytschko, and G.C. Schatz, *Computational studies of the structure, behavior upon heating, and mechanical properties of graphite oxide.* Journal of Physical Chemistry C, 2007. **111**(49): p. 18099-18111.

98. Hadzi, D. and A. Novak, *Infra-red Spectra of Graphitic Oxide.* Trans. Faraday Soc., 1955. **51**: p. 1614

99. Zhang, J., et al., *Surface-modified carbon nanotubes catalyze oxidative dehydrogenation of n-butane.* Science, 2008. **322**(5898): p. 73-77.

100. Wang, S., et al., *High Mobility, Printable, and Solution-Processed Graphene Electronics.* Nano Letters, 2009.

101. López, V., et al., *Chemical Vapor Deposition Repair of Graphene Oxide: A Route to Highly-Conductive Graphene Monolayers* Adv. Mater., 2009. **21**: p. 4683-4686.

102. Rubin, Y., C.B. Knobler, and F. Diederich, *Precursors to the cyclo[n]carbons: from 3,4-dialkynyl-3-cyclobutene-1,2-diones and 3,4-dialkynyl-3-cyclobutene-1,2-diols to cyclobutenodehydroannulenes and higher oxides of carbon.* J. Am. Chem. Soc., 2002. **112**(4): p. 1607-1617.

103. Ravagnan, L., et al., *Cluster-beam deposition and in situ characterization of carbyne-rich carbon films.* Phys. Rev. Lett., 2002. **89**(28): p. 285506.

104. Amanda, S.B. and K.S. Ian, *Thermal stability of graphene edge structure and graphene nanoflakes.* J. Chem. Phys., 2008. **128**(9): p. 094707.

105. Jin, C., et al., *Deriving Carbon Atomic Chains from Graphene.* Phys. Rev.Lett., 2009. **102**(20): p. 205501.

106. Yang, Y., W. Liu, and M. Asheghi, *Thermal and electrical characterization of Cu/CoFe superlattices.* Applied Physics Letters, 2004. **84**(16): p. 3121-3123.

107. Rangel, N.L. and J.A. Seminario, *Graphene Terahertz Generators for Molecular Circuits and Sensors.* Journal of Physical Chemistry A, 2008. **112**(51): p. 13699-13705.

108. Wang, H., et al., *Graphene Frequency Multipliers.* Ieee Electron Device Letters, 2009. **30**(5): p. 547-549.

109. Dragoman, M., et al., *Microwave switches based on graphene.* Journal of Applied Physics, 2009. **105**(5): p. 054309.

110. Rana, F., *Graphene terahertz plasmon oscillators.* Ieee Transactions on Nanotechnology, 2008. **7**(1): p. 91-99.

111. Geim, A.K., *Graphene: Status and Prospects.* Science, 2009. **324**(5934): p. 1530-1534.

112. Yazyev, O.V. and S.G. Louie, *Topological defects in graphene: Dislocations and grain boundaries.* Physical Review B, 2010. **81**(19): p. 195420.

113. Liu, Y.Y. and B.I. Yakobson, *Cones, Pringles, and Grain Boundary Landscapes in Graphene Topology.* Nano Letters, 2010. **10**(6): p. 2178-2183.

114. Malola, S., H. Hakkinen, and P. Koskinen, *Structural, chemical, and dynamical trends in graphene grain boundaries.* Physical Review B, 2010. **81**(16): p. 165447.

115. Grantab, R., V.B. Shenoy, and R.S. Ruoff, *Anomalous Strength Characteristics of Tilt Grain Boundaries in Graphene.* Science, 2010. **330**(6006): p. 946-948.

116. Huang, P.Y., et al., *Grains and grain boundaries in single-layer graphene atomic patchwork quilts.* Nature, 2011. **469**(7330): p. 389-392.

117. Kim, K., et al., *Grain Boundary Mapping in Polycrystalline Graphene.* Acs Nano, 2011. **5**(3): p. 2142-2146.

118. Bagri, A., et al., *Thermal transport across Twin Grain Boundaries in Polycrystalline Graphene from Nonequilibrium Molecular Dynamics Simulations.* Nano Letters, 2011. **11**(9): p. 3917-3921.

119. Zeng, T.F. and G. Chen, *Phonon heat conduction in thin films: Impacts of thermal boundary resistance and internal heat generation.* Journal of Heat Transfer-Transactions of the Asme, 2001. **123**(2): p. 340-347.

120. Swartz, E.T. and R.O. Pohl, *Thermal-Boundary Resistance.* Reviews of Modern Physics, 1989. **61**(3): p. 605-668.

121. MullerPlathe, F., *A simple nonequilibrium molecular dynamics method for calculating the thermal conductivity.* Journal of Chemical Physics, 1997. **106**(14): p. 6082-6085.

122. Muller-Plathe, F. and D. Reith, *Cause and effect reversed in non-equilibrium molecular dynamics: an easy route to transport coefficients.* Computational and Theoretical Polymer Science, 1999. **9**(3-4): p. 203-209.

123. Schelling, P.K., S.R. Phillpot, and P. Keblinski, *Kapitza conductance and phonon scattering at grain boundaries by simulation.* Journal of Applied Physics, 2004. **95**(11): p. 6082-6091.

124. Lindsay, L. and D.A. Broido, *Optimized Tersoff and Brenner empirical potential parameters for lattice dynamics and phonon thermal transport in carbon nanotubes and graphene.* Physical Review B, 2010. **81**(20): p. 205441.

125. Lindsay, L., D.A. Broido, and N. Mingo, *Diameter dependence of carbon nanotube thermal conductivity and extension to the graphene limit.* Physical Review B, 2010. **82**(16): p. 161402.

126. Haskins, J., et al., *Control of Thermal and Electronic Transport in Defect-Engineered Graphene Nanoribbons.* Acs Nano, 2011. **5**(5): p. 3779-3787.

127. Plimpton, S., *Fast Parallel Algorithms for Short-Range Molecular-Dynamics.* Journal of Computational Physics, 1995. **117**(1): p. 1-19.

128. Schelling, P.K., S.R. Phillpot, and P. Keblinski, *Comparison of atomic-level simulation methods for computing thermal conductivity.* Physical Review B, 2002. **65**(14): p. 144306.

129. Zhang, G. and B.W. Li, *Thermal conductivity of nanotubes revisited: Effects of chirality, isotope impurity, tube length, and temperature.* Journal of Chemical Physics, 2005. **123**(11): p. 114714.

130. Ghosh, S., et al., *Extremely high thermal conductivity of graphene: Prospects for thermal management applications in nanoelectronic circuits.* Applied Physics Letters, 2008. **92**(15): p. 151911.

131. Klemens, P.G., *Theory of thermal conduction in thin ceramic films.* International Journal of Thermophysics, 2001. **22**(1): p. 265-275.

132. Sellan, D.P., et al., *Size effects in molecular dynamics thermal conductivity predictions.* Physical Review B, 2010. **81**(21): p. 214305.

133. Nika, D.L., et al., *Phonon thermal conduction in graphene: Role of Umklapp and edge roughness scattering.* Physical Review B, 2009. **79**(15): p. 155413.

134. Kong, B.D., et al., *First-principles analysis of lattice thermal conductivity in monolayer and bilayer graphene.* Physical Review B, 2009. **80**(3): p. 033406.

135. Jauregui, L.A., et al., *Thermal Transport in Graphene Nanostructures: Experiments and Simulations.* ECS Transactions, 2010. **28**(5): p. 73-83.

136. Ong, Z.Y. and E. Pop, *Effect of substrate modes on thermal transport in supported graphene.* Physical Review B 2011. **84**(7): p. 075471.

137. Angadi, M.A., et al., *Thermal transport and grain boundary conductance in ultrananocrystalline diamond thin films.* Journal of Applied Physics, 2006. **99**(11): p. 114301.

138. Maiti, A., G.D. Mahan, and S.T. Pantelides, *Dynamical simulations of nonequilibrium processes - Heat flow and the Kapitza resistance across grain boundaries.* Solid State Communications, 1997. **102**(7): p. 517-521.

139. Samvedi, V. and V. Tomar, *The role of interface thermal boundary resistance in the overall thermal conductivity of Si-Ge multilayered structures.* Nanotechnology, 2009. **20**(36): p. 365701.

140. Nika, D.L., et al., *Lattice thermal conductivity of graphene flakes: Comparison with bulk graphite.* Applied Physics Letters, 2009. **94**(20): p. 203103.

141. Balandin, A.A., et al., *Superior thermal conductivity of single-layer graphene.* Nano Letters, 2008. **8**(3): p. 902-907.